Calorimetric and small angle x-ray scattering study of phase transitions in octylcyanobiphenyl-aerosil dispersions

G. S. Iannacchione and C. W. Garland
Department of Chemistry and Center for Material Science and Engineering, Massachusetts Institute of Technology, Cambridge, Massachusetts 02139

J. T. Mang
Manual Juan Jr. Neutron Scattering Center, Los Alamos National Laboratory, Los Alamos, New Mexico 87545

T. P. Rieker
Center for Microengineered Materials Laboratory, Department of Chemical and Nuclear Engineering, University of New Mexico, Albuquerque, New Mexico 87131

(Received 13 May 1998)

High-resolution calorimetric studies have been made of the liquid crystal phase transitions for several dispersions of 70-Å-diam silica spheres (aerosil) in octylcyanobiphenyl (8CB) as a function of silica density ρ_S. The excess specific heat peaks associated with the nematic-isotropic (N-I) and the nematic–smectic-A (N-SmA) transitions both exhibit shifts to lower temperatures, decreases in the specific heat maximum values, and decreases in the transition enthalpies as ρ_S is increased. Two distinct regimes of ρ_S-dependent behaviors are observed with a crossover between them at $\rho_S \cong 0.1$ g cm^{-3}. For lower silica densities, sharp second-order C_p peaks are observed at the N-SmA transitions, characterized by effective critical exponents that decrease monotonically with ρ_S from the pure 8CB value toward the three-dimensional XY value, and two closely spaced but distinct first-order C_p features are observed at the N-I transition. For higher silica densities, both the N-SmA and the N-I transitions exhibit a single rounded C_p peak, shifting in temperature and decreasing in total enthalpy in a manner similar to that observed in 8CB+aerogel systems. Small angle x-ray scattering data are qualitatively aerogel-like and yield temperature-independent mass-fractal dimensionalities for aerosil aggregates that differ for samples with silica densities above and below the crossover density.
[S1063-651X(98)11711-7]

PACS number(s): 61.30.−v, 64.70.Md, 82.70.Gg

I. INTRODUCTION

In the past few years, a variety of optical, x-ray, and calorimetric studies have been made of the phase behavior of liquid crystals (LCs) confined in randomly interconnected porous media [1–9]. These have included several calorimetric investigations of phase transitions for liquid crystals in silica aerogels [6–9]. Recently, the effect of dispersed silica aerosil particles on the critical nematic (N)–smectic-A (SmA) heat capacity of octylcyanobiphenyl (8CB) was reported [10]. A review and discussion of several elementary theories (finite-size effects, single-pore models, and simple random-field models inspired by magnetic systems) are given in Refs. [4], [6], and [10], but a better and more realistic theory is needed. Recent theories of the effects of quenched disorder on smectic liquid crystals by Radzihovsky and Toner [11] have produced promising results for aerogel systems. However, aerosil systems involve partially annealed elastic-strain disorder and will require separate theoretical treatment.

Aerosil systems are particularly attractive since random disorder is introduced in a controlled manner. For aerosil dispersions, silica densities comparable to those for a LC confined in aerogels can be achieved, but with greater variability and ease of sample preparation. In contrast, ''rigid'' aerogel confinement of a LC is possible for only a few densities due to limited aerogel availability. Also, the fragility of very-low-density aerogels is of concern since these are difficult to fill and the crystallization of a LC can significantly damage the aerogel structure [9].

In the initial aerosil work, the systems were prepared by mechanical mixing and the maximum value of the density ρ_S, in grams of SiO_2 per cm^3 of LC, was limited to $\sim$0.17 due to the high viscosity of LC+aerosil mixtures even when the LC is in the isotropic phase. Furthermore, there were concerns about heterogeneity in the aerosil concentration at the highest aerosil densities. A solvent preparation method has been developed that allows one to make well-mixed LC +aerosil systems with densities up to $\rho_S \approx 0.5$ g cm^{-3} or greater [12]. This method has been used to study the heat capacity of two nO-m+aerosil systems: butyloxybenzlidene octylaniline (4O.8), which exhibits the CrB-SmA-N-I phase sequence [12], and heptyloxybenzilidene butylaniline (7O.4), which exhibits a CrG-SmC-SmA-N-I sequence [13]. The symbols I, SmC, CrB, and CrG denote isotropic, smectic-C, plastic crystal-B, and tilted plastic crystal-G phases.

The present paper uses this preparation technique to investigate the high-resolution, low-frequency ac heat capacity of 8CB+aerosil systems as a function of ρ_S from 0.02 to 0.44 g cm^{-3}. Detailed measurements also have been made with nonadiabatic scanning (NAS) calorimetry, which allows the evaluation of latent heats. This study examines the thermal behavior at the N-I transition (which was previously

erratic with mechanically mixed systems), confirms the reported evolution [10,12] of the N-SmA critical C_p peak as the aerosil density increases, and reveals subtle differences between the behavior of LC+aerogel and LC+aerosil systems that were obscured in the initial work. In addition, small angle x-ray scattering (SAXS) data have been acquired for the aerosil particles alone and aerosils suspended in 8CB in order to determine the structure of the aerosil network within the LC matrix and the influence of the LC phases on this structure.

Section II describes the experimental calorimetric procedures and reports the results of C_p measurements on six 8CB +type 300 aerosil samples. The essential features are (i) shifts to lower temperatures of the C_p peaks at the N-I and N-SmA transitions, (ii) N-I pretransitional wings that are independent of ρ_S in size and shape, (iii) a two-phase $N+I$ coexistence region that exhibits two C_p peaks at low ρ_S (≤ 0.1 g cm^{-3}) and a single broad peak at large ρ_S (>0.1 g cm^{-3}) with the latter similar to that seen in 8CB+aerogel samples, (iv) N-SmA C_p peaks that remain singular for $\rho_S \leq 0.1$ g cm^{-3} but vary in size and shape such that the effective critical exponent α crosses over from a pure 8CB value of $\alpha=0.3$ toward the three-dimensional (3D) XY value of $\alpha_{XY}=-0.007$ [14] as ρ_S increases, and (v) an aerogel-like rounding of the N-SmA peak when $\rho_S > 0.1$ g cm^{-3}. Section III describes the hydrogen-bonded gel network structures that are formed in all the investigated 8CB+aerosil systems. Experimental SAXS procedures are given and scattering results are reported and analyzed for several 8CB+aerosil samples used in the present calorimetric work. The discussion in Sec. IV describes the weakly first-order N-I transition behavior in terms of the effects of a quenched random surface field and long-range elastic-strain deformations that cause a decrease in the N-I latent heat, a shift in T_{NI}, and a doubling of the effective C_p peak in the coexistence region. The evolution of N-SmA critical behavior is discussed in terms of a quenched random surface field with quasiannealed elastic strain at low ρ_S followed by elastic-strain effects with surface induced local order at higher ρ_S. Several features of these 8CB+aerosil samples indicate a change at $\rho_S \approx 0.1$ g cm^{-3} from a ''soft gel'' regime to an aerogel-like ''stiff gel'' regime. Section V summarizes the conclusions to be drawn from these and other LC+aerosil studies.

II. CALORIMETRIC PROCEDURES AND RESULTS

A. Procedures

The 8CB used in the present study was obtained from Merck/BDH Corp.; it is not from the same synthetic batch as that used in Ref. [10]. This compound ($M=291.44$ g mol^{-1}) has the structural formula

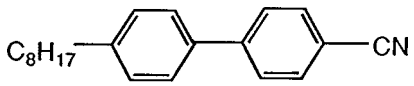

and exhibits the phase sequence [15]

$$\underset{}{\mathrm{Cr}K} \underset{290\ \mathrm{K}}{\text{——}} \mathrm{Sm}A \underset{306.9\ \mathrm{K}}{\text{——}} N \underset{313.9\ \mathrm{K}}{\text{——}} I,$$

where CrK is the rigid crystal form. The SmA-CrK transition temperature is suppressed substantially in 8CB+aerosil and 8CB+aerogel systems [16] and will not be studied in the present investigation. A hydrophilic aerosil (type 300), obtained from Degussa Corp. [17], was used after drying under vacuum at $\sim$200 °C overnight. This sil consists of 70-Å-diam SiO_2 spheres with hydroxyl groups covering the surface and a specific surface area of $a=300$ m^2 g^{-1} determined from a Brunauer-Emmett-Teller adsorption isotherm; see Ref. [10] for further characteristics of this aerosil.

Five 8CB+aerosil samples were prepared with the solvent method described in Ref. [12] except that chemically pure acetone was used as the solvent instead of absolute ethanol. In essence, this method involves adding the sil powder to a dilute solution of 8CB in acetone, sonicating the mixture to achieve good dispersion, and slowly evaporating off the solvent at temperatures above 315 K. The sample was then placed in a vacuum system at 10^{-3} Torr and pumped on for $\sim$12 h at 323 K. In all cases, the final 8CB+aerosil samples looked uniform to the eye, showed no significant agglomeration on inspection with a microscope, and formed thixotropic gels. In addition to those solvent prepared samples, one 8CB+aerosil sample with $\rho_S=0.124$ g cm^{-3} was prepared by the mechanical mixing method used in Ref. [10]. This was done to allow a comparison of the effects of preparation technique and to make contact with the results of the earlier study.

The calorimetric measurements were carried out at MIT. After a sample was prepared and allowed to cool to room temperature under vacuum, it was cold-weld sealed (with indium) into a silver cell ($\sim$1 cm diameter and $\sim$0.05 cm thick) under dry nitrogen with the total exposure to the ambient atmosphere being less than 1 min. The filled cell was then mounted in a high-resolution calorimeter capable of operation in either ac or NAS modes as described elsewhere [18–20]. The equations for processing the observed ac mode responses [$|T_{\mathrm{ac}}|$ and $\varphi \equiv \Phi + \pi/2$, where Φ is the phase shift of $T_{\mathrm{ac}}(\omega)$ with respect to the input power $P_{\mathrm{ac}} \exp(i\omega t)$] are given in Ref. [19]. The essential equations for ac calorimetry are

$$C_p = [C'_{\mathrm{filled}} - C_{\mathrm{empty}}]/m = [(P_{\mathrm{ac}}/\omega|T_{\mathrm{ac}}|)\cos\varphi - C_{\mathrm{empty}}]/m, \tag{1}$$

$$C''_{\mathrm{filled}} = (P_{\mathrm{ac}}/\omega|T_{\mathrm{ac}}|)\sin\varphi - 1/\omega R, \tag{2}$$

where C'_{filled} and C''_{filled} are the real and imaginary components of the heat capacity, C_{empty} is the heat capacity of the empty silver cell plus SiO_2, m is the mass of LC in grams (typically 20–30 mg), and R is the thermal resistance between the cell and the bath (typically 180 K W^{-1}). Equations (1) and (2) are not strictly correct for samples with a nonnegligible internal thermal resistance compared to R, however, the required correction (applied to all data presented here) typically results in a small shift in the background heat capacity value [18,19]. Measurements were made over a wide frequency range, $2\omega_0$ to $\omega_0/20$ for some samples, where $\omega_0=0.1963$ s^{-1} ($f_0=\omega_0/2\pi=31.25$ mHz) is the standard operating frequency used for most of the previous work with this calorimeter. For all data in one-phase regions (i.e., everywhere except close to T_{NI}, where there is two-phase coexistence), static C_p values are shown. That is, data were obtained at sufficiently low frequencies so that C_p was inde-

pendent of ω and $C''_{\text{filled}}=0$. All data shown here were obtained on cooling at scan rates $|dT/dt|$ of less than 100 mK h^{-1}. Heating data were in good agreement, with a small hysteresis of $\sim$0.05 K for the N-I transition temperature. The phase transition temperatures were extremely stable: Typical drifts in T_{NI} were estimated at -4 mK per day and drifts in T_{NA} were even less.

In addition to ac calorimetry, several nonadiabatic scanning calorimetry runs were carried out. Basically, this technique is a modification of relaxation calorimetry that involves linearly ramping the dc heater power $P(t)$ while the bath temperature is held constant. The effective heat capacity C_{eff} is inversely proportional to the time derivative of the temperature response and contains contributions from both the pretransitional C_p wings and the latent heat ΔH in the case of first-order transitions. Details of this technique can be found elsewhere [19,20]. Measurements were performed on cooling over a 6 K temperature range about the N-I transition temperature on three 8CB+aerosil samples at a scan rate of -109 mK $min^{-1}=-6.5$ K h^{-1}.

B. Results

The heat capacity of the pure liquid crystal was determined for our 8CB samples. These data are not shown, but the resulting C_p values were in excellent agreement with several previously published calorimetric studies of 8CB [6,10,5,21]. The best data on pure 8CB are those of Thoen, Marynissen, and Van Dael [15], who give T_{NI}(pure) $=313.92$ K and T_{NA}(pure)$=306.92$ K. The transition temperature values for our 8CB sample were T_{NI}(pure) $=313.98$ K (center of a 60-mK-wide coexistence region) and T_{NA}(pure)$=306.97$ K.

Figure 1 shows as a typical example the C_p(ac) variation over an extended temperature range for the 8CB+aerosil sample with $\rho_S=0.092$ g cm^{-3}. Data were obtained for this sample at eight frequencies between $2\omega_0$ ($f=62.5$ mHz) and $\omega_0/20$ ($f=1.56$ mHz). No frequency dependence was observed for C_p for $\omega\leqslant\omega_0/4$, except in the two-phase $N+I$ coexistence region, which was the only region where the imaginary part $C''_{\text{filled}}\neq 0$. Thus the data in Fig. 1 represent the static C_p values except for those points near T_{NI} denoted with crosses. The C_p behavior shown here is typical of other 8CB+aerosil samples in that the N-SmA peak is very sensitive in shape and size to ρ_S. For comparison, the maximum C_p value observed at T_{NA} for pure 8CB is $\sim$5 J K^{-1} g^{-1} [15]. The smooth dashed curve directly under the N-SmA heat capacity peak represents C_p(base line), which represents the C_p variation expected in the absence of a N-SmA transition. This is used to determine the excess heat capacity associated with the N-SmA transition

$$\Delta C_p(NA)=C_p-C_p(\text{baseline}). \tag{3}$$

The linear dash-dotted line is C_p(background) used to obtain $\Delta C_p(NI)$ from

$$\Delta C_p(NI)=C_p(NI)-C_p(\text{background}), \tag{4}$$

where $C_p(NI)$ is the observed heat capacity when T is far from T_{NA} and the dashed N-SmA ''baseline'' curve near T_{NA}. One can define an integrated pretransitional enthalpy δH with

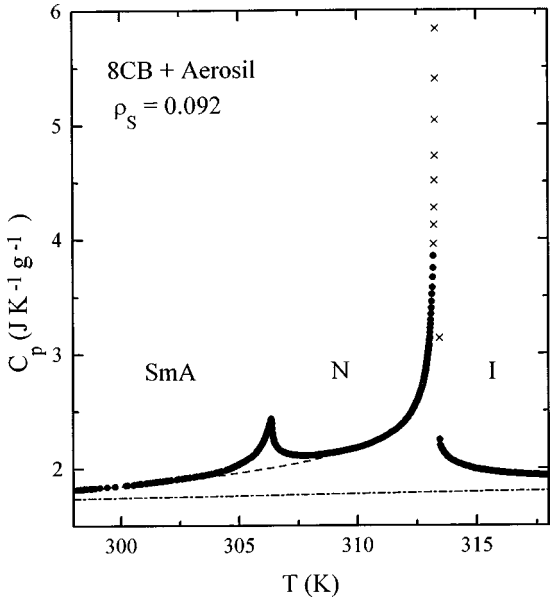

FIG. 1. Specific heat capacity obtained with an ac calorimeter over a 20-K temperature range for an 8CB+aerosil sample with $\rho_S=0.092$ g cm^{-3}. These data were obtained at $\omega_0/6$ ($f=5.208$ mHz). The dash dotted line represents the background C_p, while the dashed curve represents the low temperature N-I C_p wing that would be expected in the absence of the N-SmA transition. The latter acts as C_p(baseline) for the N-SmA transition. Crosses indicate points obtained in a region of $N+I$ phase coexistence.

$$\delta H=\int \Delta C_p dT. \tag{5}$$

For a second-order or continuous transition, the integration covers the entire ΔC_p peak over as wide a temperature range as possible and yields the total enthalpy change associated with the transition. For a first-order transition, the integration is more complicated due to two-phase (e.g., $N+I$) coexistence and the presence of a latent heat ΔH. Typically, the C_p(ac) values obtained in a two-phase coexistence region are artificially high and frequency dependent due to partial phase conversion (e.g., $N\leftrightarrow I$) during a T_{ac} cycle. In order to obtain the N-I pretransitional enthalpy contribution δH_{NI}, we have truncated the $\Delta C_p(NI)$ values in the coexistence region with a linear variation between the highest-temperature frequency-independent N phase point and the lowest-temperature frequency-independent I phase point. This will be illustrated later in Fig. 3. Note that a complete integration over the entire ΔC_p peak (including the anomalous effective heat capacity points in the two-phase coexistence region) includes *some* of the latent heat contribution and yields an effective enthalpy change denoted by δH^*, where $\delta H<\delta H^*<\delta H+\Delta H$. The total transition enthalpy for weakly first-order transitions is given by

$$\Delta H_{\text{tot}}=\delta H+\Delta H, \tag{6}$$

TABLE I. Position and magnitude of $\Delta C_p(NI)$ and $\Delta C_p(NA)$ peaks for pure 8CB and 8CB+aerosil samples with silica density ρ_S in g cm^{-3}. T_{NI} denotes the cnter of a $N+I$ coexistence region of width NI(coex) and T_{NA} denotes the peak position of $\Delta C_p(NA)$, which is not necessarily the same as T_C obtained from power-law fits. All temperature values are in K. δH^*_{NI} represents the effective integrated ac enthalpy (which includes *part* of the latent heat), ΔH_{NI} is the latent heat, and $\Delta H_{\rm tot}(NI)=\delta H_{NI}+\Delta H_{NI}$ is the total transition enthalpy of the N-I transition. Note that δH_{NI} is 5.58 J g^{-1} for pure 8CB [10] and 5.43 J g^{-1} for all 8CB+aerosil samples. δH_{NA} is the integrated ac enthalpy for the N-SmA transition. All enthalpies are in J g^{-1}.

Sample	ρ_S	T_{NI}	NI(coex)	T_{NA}	δH^*_{NI}	ΔH_{NI}	$\Delta H_{\rm tot}(NI)$	δH_{NA}
Pure 8CB	0	313.98	0.06	306.970		2.10[a]	7.68[a]	0.80[a]
8CB+aerosil	0.022	313.19	0.20	306.220	6.76			0.72
	0.052	313.04	0.22	306.124	6.50	1.97	7.40	0.58
	0.092	313.39	0.25	306.378	6.38			0.47
	0.124[b]	313.31	~0.14	306.45	6.51			0.61
	0.183	313.21	0.26	306.0	6.33	1.57	7.00	0.41
	0.436	312.41	~0.58	304.9	5.96	0.72	6.15	0.34

[a]References [5,10,15].

[b]Mechanically mixed sample.

where $\Delta H_{\rm tot}$ can be obtained from nonadiabatic scanning calorimetry and ΔH is the latent heat.

One important aspect of the N-I transition in 8CB +aerosil samples is the fact that the size and shape of the pretransitional wings $\Delta C_p(NI)$ are independent of ρ_S in spite of significant shifts in the T_{NI} transition temperatures and decreases in the effective integrated ac enthalpy δH^*_{NI} with increasing ρ_S, as given in Table I. Figure 2 shows a superposition of $\Delta C_p(NI)$ data versus $T-T_{NI}$ for five 8CB +aerosil samples. Data are not shown for pure 8CB or for the mechanically mixed aerosil sample (ρ_S $=0.124$ g cm^{-3}), but $\Delta C_p(NI)$ wings for these agree very well with those shown in Fig. 2. This invariance of $\Delta C_p(NI)$

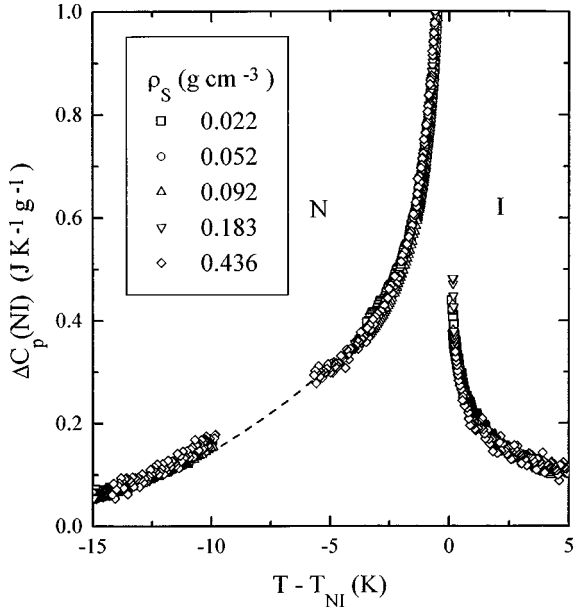

FIG. 2. Superpositions of $\Delta C_p(NI)$ for five solvent-prepared 8CB+aerosil samples. Data in the N-SmA transition region have been omitted for clarity and the dashed line is the dashed C_p(base line) curve shown in Fig. 1. Note the nearly perfect overlap of data points.

wings is also observed for 4O.8+aerosils [12]. In that system, $\Delta C_p(NI)$ for hydrophilic aerosil samples match the pure 4O.8 $\Delta C_p(NI)$ wings for ρ_S values in the investigated range 0.028–0.438 g cm^{-3} and the two-phase coexistence width varied from 0.27 to ~0.4 K. In the case of 8CB +aerogels [6], the $\Delta C_p(NI)$ wings are smaller than the bulk values over the range $-0.9\ {\rm K}<T-T_{NI}<0.4\ {\rm K}$ for ρ_S $=0.455$ and $-2.5\ {\rm K}<T-T_{NI}<0.7$ K for $\rho_S=0.825$. Thus a rigid aerogel structure with a ρ_S value greater than roughly 0.3 g cm^{-3} perturbs the N-I transition more than does the ''stiff'' gel formed by aerosil particles.

In contrast to the behavior of the N-I pretransitional wings shown in Fig. 2, the ac calorimetric data for 8CB +aerosils in the two-phase $N+I$ coexistence region are very sensitive to ρ_S. Pure 8CB has a 60-mK-wide coexistence region characterized by a large, sharp peak in the apparent C_p and also a peak in $C''_{\rm filled}$ values that reflects well known phase-shift anomalies at the weakly first-order N-I transition [18,22]. Figure 3 shows the $\Delta C_p(NI)$ behavior for pure 8CB and four solvent prepared 8CB+aerosil samples in the immediate vicinity of T_{NI}. There is a double feature in the coexistence region for aerosil samples with ρ_S $\leqslant 0.1$ g cm^{-3}, which is mirrored by the behavior of the imaginary component $C''_{\rm filled}$: a sharp peak followed at lower temperature by a more rounded peak. For larger values of ρ_S, both $\Delta C_p(NI)$ and $C''_{\rm filled}$ exhibit broad single coexistence peaks. Except for the $N+I$ coexistence region, $C''_{\rm filled}$ equals zero over a wide temperature range, as expected for one-phase data in the absence of dynamical effects. The two C_p peaks in the coexistence region lie at 313.23 and 313.15 K for $\rho_S=0.022$ and 313.08 K, 312.92 K for $\rho_S=0.052$, and 313.42 and 313.34 K for $\rho_S=0.092$ g cm^{-3}. The difference in temperature between these two peaks is 0.08–0.16 K and shows no systematic trend with ρ_S. With increasing ρ_S, the low-temperature peak increases in intensity slowly while the sharper high-temperature peak loses intensity rapidly, as shown in Fig. 3. Note that the slanted dashed lines in Fig. 3 indicate the C_p truncation in the two-phase region used to determine δH_{NI}. The shaded region in the first panel of Fig.

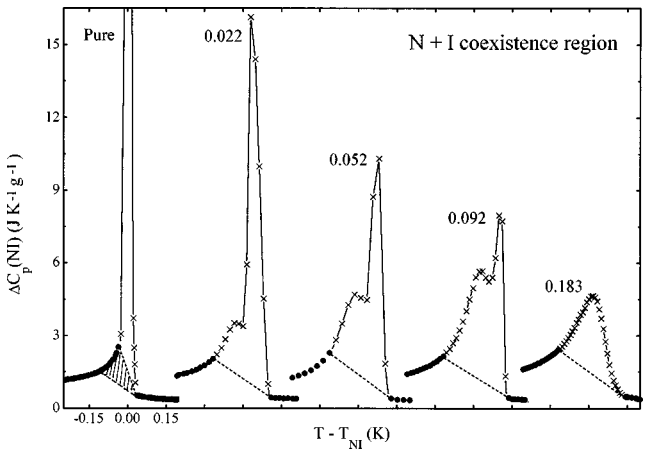

FIG. 3. $\Delta C_p(NI)$ for pure 8CB and four 8CB+aerosil samples (ρ_S values in g cm^{-3} indicated in the figure) over a 0.45-K temperature range about T_{NI} concentrating on the $N+I$ coexistence region ($\times$). The ΔC_p coexistence values for the $\rho_s=0.436$ 8CB +aerosil sample (not shown) are somewhat smaller, but otherwise have a shape identical to that for the $\rho_S=0.183$ sample. Note the double $\Delta C_p(NI)$ feature for $\rho_S<0.1$ g cm^{-3}. The slanting dashed lines show the truncations used to obtain δH_{NI}, whereas δH^*_{NI} is obtained by integrating over all the ac points.

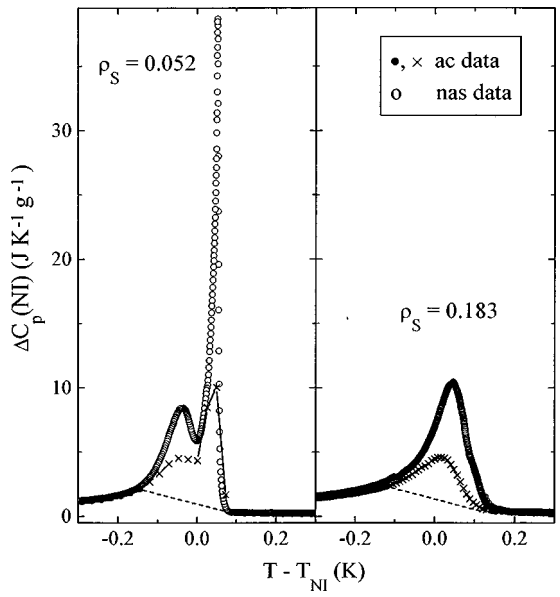

FIG. 4. Detailed view of $\Delta C_p(NI)$ obtained near T_{NI} with both ac calorimetry (at $\omega_0/6$) and nonadiabatic scanning (NAS) calorimetry for two 8CB+aerosil samples. The slanting dashed lines connecting one-phase ac data points were used to evaluate δH_{NI}. The integral of the nonadiabatic scan data yields $\Delta H_{\rm tot}(NI)$ and the latent heat $\Delta H_{NI}=\Delta H_{\rm tot}(NI)-\delta H_{NI}$ is the NAS area lying above the dashed line.

3 indicates the portion of the pretransitional enthalpy δH_{NI} for pure 8CB that is missing from δH_{NI} of the aerosil samples but is now included in the broader two-phase coexistence region of the 8CB+aerosil samples.

In the case of N-I transitions, latent heat effects associated with the partial interconversion of coexisting N and I phases are the cause of the artificially large effective C_p(ac) values in the two-phase regions shown in Figs. 1 and 3. The δH^*_{NI} values obtained from ac calorimetry by integrating over ΔC_p(ac) values including those in the coexistence region are lower bounds on the total enthalpy $\Delta H_{\rm tot}$. Nonadiabatic scanning data ΔC_p(NAS), the integration of which yields $\Delta H_{\rm tot}$ makes it possible to determine the latent heat ΔH since δH can be obtained from truncated ΔC_p(ac) data. Figure 4 shows an overlay of $\Delta C_p(NI)$ from nonadiabatic scanning and ac calorimetry for two 8CB+aerosil samples. Clearly, there is latent enthalpy associated with both $C_p(NI)$ peaks observed for the low-ρ_S sample, although partitioning $\Delta H_{\rm tot}$ between them is impossible. The doubling disappears for $\rho_S>0.1$ g cm^{-3} and ΔH diminishes as ρ_S increases, as seen by the 0.183-g cm^{-3} sample in Fig. 4 and the 0.436-g cm^{-3} sample (not shown).

The $\Delta C_p(NI)$ behavior for the one mechanically mixed sample with $\rho_S=0.124$ g cm^{-3} (not included in Fig. 3) was determined in order to explore the influence of the preparation technique. In this sample, there is also a double C_p peak observed near T_{NI}, but the separation between the two features at 313.34 and 313.03 K is much larger than for the solvent-prepared samples. Furthermore, anomalous phase shift values leading to $C''_{\rm filled}>0$ are limited to the region of the high-temperature peak. Thus two-phase coexistence does not span both peaks as it does in Fig. 3. Moreover, the size of the lower-temperature peak is much smaller and both peak temperatures are less shifted with respect to pure 8CB than is observed for the solvent-prepared samples. This supports the suggestion put forth in Ref. [10] that mechanical mixing does not reliably and reproducibly create a uniform dispersion of aerosil particles.

The behavior of $\Delta C_p(NA)$ as a function of aerosil concentration is dramatically different from that of $\Delta C_p(NI)$, as shown in Fig. 5. The N-SmA peak is not doubled in any sample studied, but the size and shape of this peak are sensitive to ρ_S. As observed in Refs. [10] and [12], when the

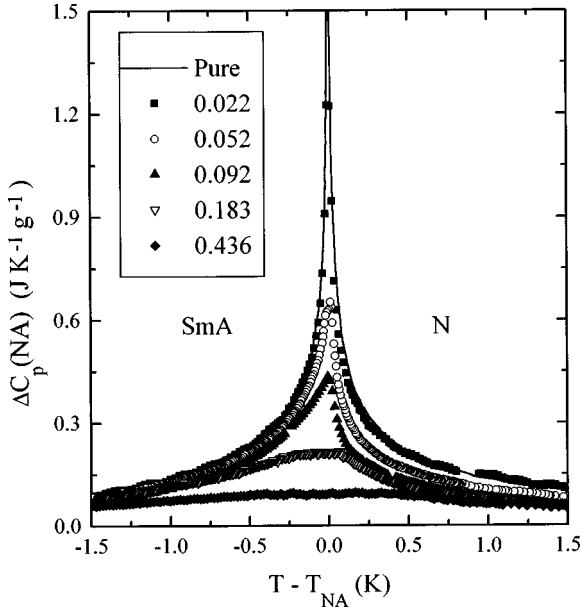

FIG. 5. $\Delta C_p(NA)$ for pure 8CB and five solvent-prepared 8CB +aerosil samples over a 3-K-wide window about T_{NA}. The ρ_S values are specified in the inset. Note the sharp and increasingly asymmetric shape as ρ_S increases from 0 (pure) to $\sim$0.1 g cm^{-3} and the aerogel-like rounding for larger ρ_S.

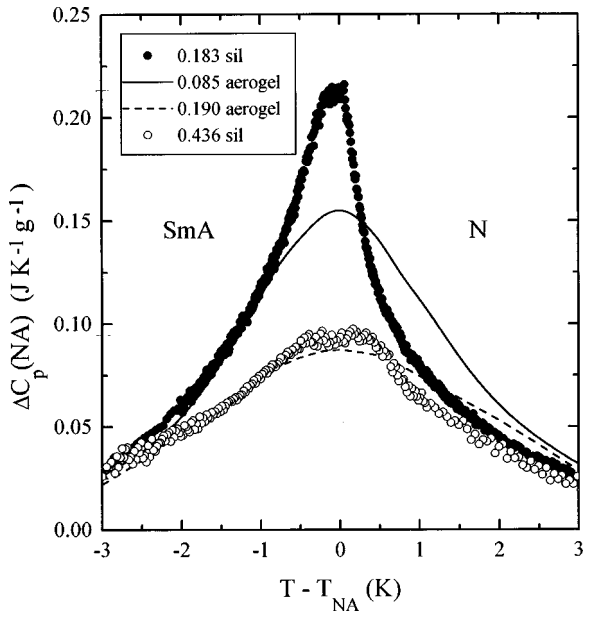

FIG. 6. Comparison of $\Delta C_p(NA)$ for the $\rho_S=0.183$ and 0.436 g cm^{-3} 8CB+aerosil samples and the $\rho_S=0.085$ and 0.189 g cm^{-3} 8CB+aerogel samples from Ref. [6]. Despite its truncated appearance in Fig. 5, the $\rho_S=0.183$ sil peak is much sharper than the peak observed in the less dense 0.085 aerogel sample.

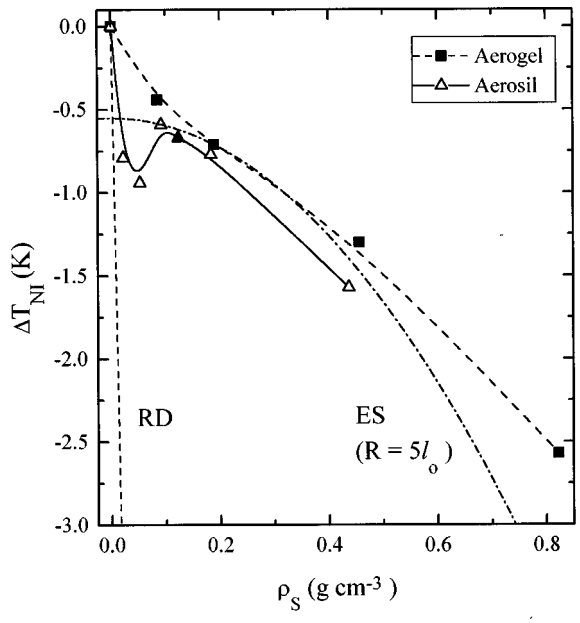

FIG. 7. Comparison of the N-I transition temperature shift $\Delta T_{NI}=T_{NI}-T_{NI}$(pure) for six 8CB+aerosil samples and four 8CB +aerogel samples from Ref. [6]. The mechanically mixed 8CB +aerosil sample is shown by the filled triangle. The uncertainty is estimated to be $\sim$0.05 K due primarily to determining the center of the coexistence range. The dashed and solid lines are guides for the eye. The short-dashed and dash-dotted lines are calculated from random-dilution (RD) and the empirical elastic-strain (ES) models, respectively; see Sec. IV text for a discussion.

N-SmA transition is second order in a pure LC, the N-SmA excess heat capacity for LC+aerosil samples remains sharp for $\rho_S \leqslant 0.1$ g cm^{-3} and becomes rounded for higher-ρ_S values. In the regime $0<\rho_S<0.1$ g cm^{-3}, $\Delta C_p(NA)$ takes on an increasingly asymmetric appearance, lower on the high-temperature side of the transition, with increasing ρ_S. This change in the shape of $\Delta C_p(NA)$ is the same as the evolution of ΔC_p toward a 3D XY-type N-SmA behavior as observed in the aerosil study of Zhou *et al.* [10]. The rounding of $\Delta C_p(NA)$ for $\rho_S>0.1$ aerosil sample is qualitatively like that observed in 8CB+aerogel samples [6], as shown in Fig. 6.

Table I provides the N-I and N-SmA transition temperatures and the $N+I$ coexistence width for pure 8CB and six 8CB+aerosil samples. Included are values of the enthalpies δH^*_{NI} and δH_{NA} as well as some values for $\Delta H_{\rm tot}(NI)$ and the latent heat ΔH_{NI}. Note that with the truncations illustrated in Figs. 3 and 4, δH_{NI} is independent of ρ_S and has the value 5.43 J g^{-1} for all 8CB+aerosil samples, which is consistent with Fig. 2. Thus the latent heat ΔH_{NI} can be determined from the total N-I transition enthalpy $\Delta H_{\rm tot}$ in those cases where the latter is known. No attempt has been made to partition either $\Delta H_{\rm tot}$ or ΔH_{NI} between the two $C_p(NI)$ features seen in aerosil samples with $\rho_S<0.1$ g cm^{-3}.

Figure 7 gives the N-I transition temperature shifts as a function of ρ_S for the six 8CB+aerosil samples and for four 8CB+aerogel samples from Ref. [6]. Two ρ_S-dependent regimes are evident in the aerosil samples. For $\rho_S \leqslant 0.1$ g cm^{-3} there is a very rapid shift of T_{NI} to lower temperatures, while for densities above 0.1 g cm^{-3} the shift is comparable to that seen in the 8CB+aerogel systems. Figure 8 gives the N-SmA transition temperature shifts for the same samples as a function of ρ_S. Again there is a crossover between two ρ_S-dependent aerosil regimes: a rapid shift of T_{NA}

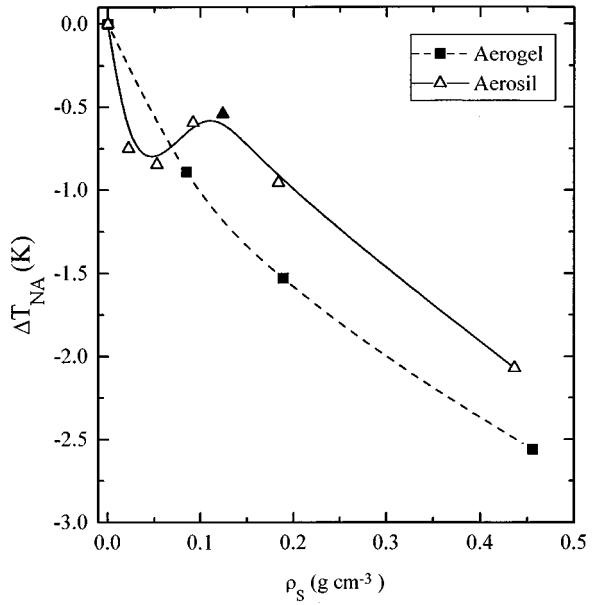

FIG. 8. Comparison of the N-SmA transition temperature shifts $\Delta T_{NA}=T_{NA}-T_{NA}$(pure) for six 8CB+aerosil samples and three 8CB+aerogel samples from Ref. [6]. No N-SmA heat capacity peak was observed in [6] for the 8CB+aerogel sample with $\rho_S=0.825$. The mechanically mixed 8CB+aerosil sample is shown by the filled triangle. The uncertainty is estimated to be $\pm$0.01 K for $\rho_S<0.1$ and $\pm$0.05 K for $\rho_S \geqslant 0.1$ due to the rounding of the $\Delta C_p(NA)$ peak. The dashed and solid lines are guides for the eye.

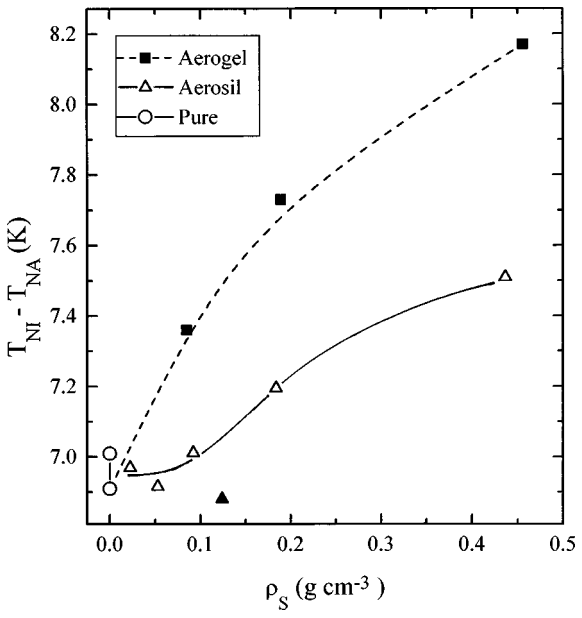

FIG. 9. Width of the nematic range $T_{NI}-T_{NA}$ as a function of ρ_S for six 8CB+aerosil samples and three 8C+aerogel samples from Ref. [6]. The mechanically mixed 8CB+aerosil sample is shown by the filled triangle. The pure values were obtained from three different samples (present data and [6,15]). The dashed and solid lines are guides for the eye.

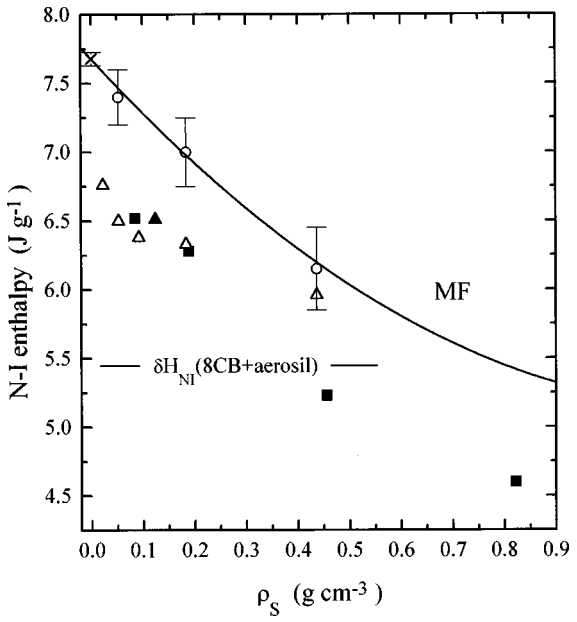

FIG. 10. N-I transition enthalpies. The quantities δH_{NI}^* for 8CB +aerosil samples (△) and for 8CB+aerogel samples (■) [6] are effective enthalpy values obtained from ac calorimetry and these represent lower bounds on the total N-I enthalpy. The mechanically mixed 8CB+aerosil sample is shown by the filled triangle. Also shown by points with error bars is the total N-I transition enthalpy $\Delta H_{\rm tot}$ for pure 8CB (×) and three 8CB+aerosil samples (○). δH_{NI} indicates the ρ_S-independent integrated area of the $\Delta C_p(NI)$ wings for 8CB+aerosil samples. See the text in Sec. IV for a discussion of the mean-field (MF) model for the suppression of the N-I latent heat.

to lower temperatures nearly identical to the shift of T_{NI} for $\rho_S \leqslant 0.1$ g cm^{-3} and a slower aerogel-like shift for larger ρ_S. This complex ρ_S dependence of ΔT_{NA} for 8CB+aerosil samples, including the decrease in $|\Delta T_{NA}|$ between $\rho_S = 0.05$ and 0.10, is confirmed by preliminary x-ray scattering experiments on this system [23]. As shown in Fig. 9, the nematic temperature range, given by $T_{NI}-T_{NA}$, is essentially constant in the low-ρ_S regime up to ~0.1 g cm^{-3} and then increases in an aerogel-like manner in the high-ρ_S regime.

Values of the N-I transition ac enthalpy δH_{NI}^* for six 8CB+aerosil samples and four 8CB+aerogel samples from Ref. [6] are shown as a function of ρ_S in Fig. 10, which also includes the total N-I transition enthalpy $\Delta H_{\rm tot}$ for pure 8CB and three of the 8CB+aerosil samples. Recall that δH_{NI} for the aerosil samples is essentially independent of ρ_S at 5.43 J g^{-1}, as described previously. As ρ_S increases, δH_{NI}^* and $\Delta H_{\rm tot}$ values for aerosil samples decrease and approach each other. This is due to a reduction in the latent heat, which influences both $\Delta H_{\rm tot}$ and the effective C_p(ac) values in the $N+I$ coexistence region that are included in the integration used to obtain δH_{NI}^*. As shown in Table I, ΔH_{NI} decreases from 2.10 J g^{-1} for pure 8CB to 0.72 J g^{-1} for the sil sample with $\rho_S = 0.436$ g cm^{-3}. For aerosil samples with larger ρ_S values, we expect that the first-order latent heat will vanish and that the value of δH_{NI} may diminish as the gel becomes progressively stiffer and more like a rigid aerogel. The absence of a N-I latent heat and a diminished δH_{NI} have been seen in 8CB+aerogel and 4O.8+aerogel samples [6,7], although the latter samples may have suffered from 4O.8 freeze fracturing of the aerogel.

The integrated enthalpy δH_{NA} for the N-SmA transition in pure 8CB, six 8CB+aerosil samples from this work, and three 8CB+aerogel samples from Ref. [6] are plotted as a function of ρ_S in Fig. 11. As seen in various other quantities, there are two ρ_S-dependent regimes for aerosil samples: δH_{NA} varying rapidly for low ρ_S and much slower for high ρ_S. The crossover between these regimes is at about 0.1 g cm^{-3}. The δH_{NA} values reported in Ref. [10] for the mechanically stirred aerosil dispersions are not shown in Fig. 11 since there is a considerable scatter in the variation of δH_{NA} as a function of ρ_S for those samples. The fact that δH_{NA} for the present mechanically mixed sample with $\rho_S = 0.124$ differs from the smooth trend of the δH_{NA} values for the solvent-sonicated samples is consistent with the behavior observed in Ref. [10]. Interestingly, the values of ΔT_{NI}, ΔT_{NA}, and δH_{NI}^* for the mechanically mixed sample are in reasonably good agreement with the trends observed for the other samples, indicating that δH_{NA} is very sensitive to the mixture homogeneity.

C. N-SmA power-law fits

A critical exponent analysis has been carried out on $\Delta C_p(NA)$ for the three 8CB+aerosil samples with $\rho_S \leqslant 0.1$ g cm^{-3} using the usual power-law form with correction-to-scaling terms [10,24]:

$$\Delta C_p = A^{\pm}|t|^{-\alpha}(1+D^{\pm}|t|^{0.5}) + B_C, \tag{7}$$

where $t \equiv (T-T_C)/T_C$ is the reduced temperature and B_C is the contribution of the singular free energy to the regular

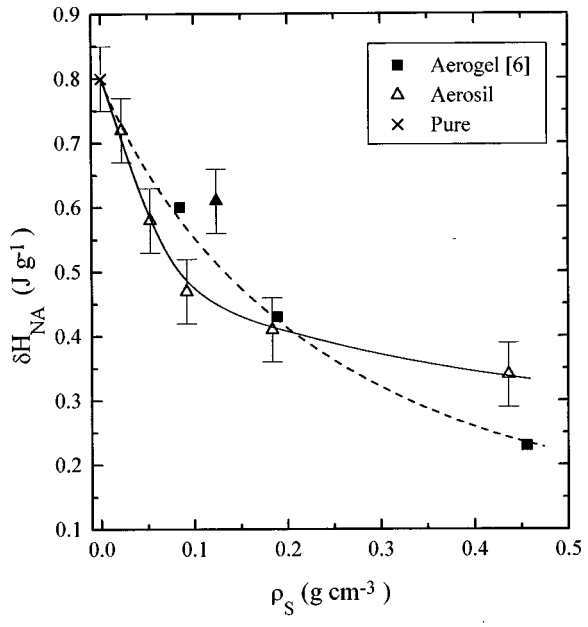

FIG. 11. Integrated enthalpy δH_{NA} for the N-SmA transition in pure 8CB, the present 8CB+aerosil samples and 8CB+aerogel samples from Ref. [6]. The mechanically mixed 8CB+aerosil sample reported in the present study is shown by the filled triangle. The lines are guides for the eye.

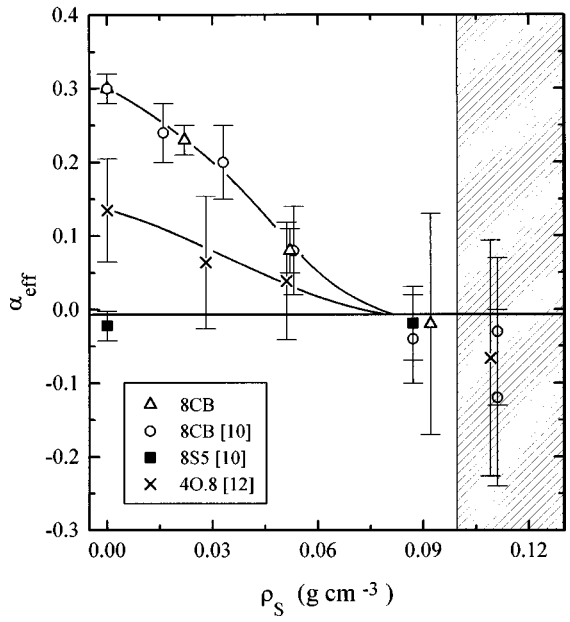

FIG. 12. Effective specific heat critical exponent α_{eff} for the second-order N-SmA transition in pure 8CB and three 8CB +aerosil mixtures (△). Also plotted are α_{eff} values for 8CB +aerosil mixtures from Ref. [10] (○), 4O.8+aerosil mixtures from Ref. [12] (×), and 8S5+aerosil mixtures from Ref. [10] (■). The shaded region above $\rho_S = 0.1$ corresponds to an aerogel-like regime where the $\Delta C_p(NA)$ peak is rounded due to strain smearing and power-law fits are marginal in quality or impossible.

heat capacity. Nonlinear least-squares fits with Eq. (7) were performed for a maximum reduced temperature $|t|_{\max} = 10^{-2}$, with range shrinking down to $\sim 5 \times 10^{-3}$ in order to test the stability of the fit parameters. Rounded data close to T_C were excluded and the minimum reduced temperature ($|t|_{\text{mm}}$) values are listed along with the final fit parameters in Table II for pure 8CB and the three lowest concentration aerosil mixture samples studied in this work.

The fitting results for the N-SmA transition in pure 8CB are consistent with the literature values of $\alpha(0) = 0.29-0.31$ and $A^-/A^+(0) = 1.00 \pm 0.08$ [15,21]. With the addition of aerosil, $\alpha(\rho_S)$ decreases smoothly to 0.08 for the $\rho_S = 0.052$ g cm^{-3} sample while the amplitude ratio A^-/A^+ remains in the range 1.05–1.08. For the $\rho_S = 0.092$ g cm^{-3} sample, the fit yields a negative critical exponent very close to zero. Since the $\Delta C_p(NA)$ data for this sample are anomalously asymmetric very near T_C, it was necessary to omit from the fit data in the range $T_C - 0.25$ to $T_C + 0.12$ K. As a result of this loose constraint on T_C, the χ^2 minimum for α is very broad. Furthermore, the fit yields a negative D^-/D^+ ratio rather than the theoretically expected $D^-/D^+ \approx +1$. This behavior indicates the approach of a breakdown of power-law behavior prior to the observation of extensive aerogel-like rounding of the $\Delta C_p(NA)$ peak. Fits were not attempted on samples that, exhibited obvious rounding effects ($\rho_S \geq 0.124$ g cm^{-3}). As shown in Fig. 12, the trend in α as a function of ρ_S is completely consistent with previous 8CB+aerosil results [10] despite differences in the sample preparation procedure. This adds support to the evolution of the critical behavior of the N-SmA transition towards 3D XY universality as ρ_S increases in the low-ρ_S regime. The change in the effective critical exponent α_{eff} from 0.30 to ~ 0 is statistically significant within 95% confidence limits.

Also shown in Fig. 12 are the evolution of the N-SmA heat capacity exponents for 4O.8+aerosil [12] and octylphenylthiolpentyloxybenzoate (8S5)+aerosil [10] samples, which clearly establish the evolution of α toward zero for $\alpha(\text{pure}) > 0$ (8CB and 4O.8) and α unchanged for $\alpha(\text{pure}) < 0$ (8S5) for increasing ρ_S. Above $\rho_S = 0.1$ g cm^{-3}, the N-SmA heat capacity peak for all LCs exhibits a broad, rounded, and greatly suppressed peak. The behaviors both

TABLE II. Least-squares parameter values from fits with Eq. (7) to $\Delta C_p(NA)$ in pure 8CB and 8CB+aerosil mixtures with silica density ρ_S in g cm^{-3}. All fits used $|t|_{\max} = 0.01$. The error bounds quoted for α_{eff} and T_C are 95% confidence limits determined by stepping α_{eff} through a series of fixed values and using the F test. The units for A^+ and B_C are J K^{-1} g^{-1}.

Sample	ρ_S	α_{eff}	T_C (K)	B_C	A^+	A^-/A^+	D^+	D^-/D^+	χ^2_ν	$10^5\|t\|_{\min}$
Pure 8CB[a]	0	0.30±0.02	306.972±0.001	−0.421	0.076	1.049	5.171	0.723	1.01	±3
8CB+aerosil	0.022	0.23±0.02	306.230±0.001	−0.497	0.141	1.072	3.256	0.663	1.06	+4/−6
	0.052	0.08±0.03	306.135±0.002	−1.480	0.940	1.078	1.269	0.191	1.19	+8/−10
	0.092	−0.02±0.15	306.319±0.020	7.072	−7.965	0.975	−0.504	−0.120	1.36	+39/−82

[a]Reference [10].

TABLE III. Characteristics of gel structures for 8CB+aerosil and 8CB+aerogel systems. Density ρ_S = g SiO_2 per cm^3 of LC; volume fraction of ''pores'' (porosity) $\phi=\rho/\rho_s$, where ρ is the density g SiO_2 per cm^3 total gel volume; mean aerosil void size $l_0=2/a\rho_s$, where a is the specific silica area (300 $m^2\ g^{-1}$ for type 300 hydrophilic aerosil); L is the average pore chord in aerogels [6]. The quantity $p=l_b a\rho_s$ is the fraction of 8CB molecules anchored by the SiO_2 surface.

Sample	ρ_s (g cm^{-3})	ϕ	l_0 (Å)	L (Å)	p[a]
Aerosil	0.022	0.990	3030	(3210)[b]	0.013
	0.052	0.977	1280	(1380)	0.031
	0.092	0.960	725	(800)	0.055
	0.124[c]	0.947	540	(600)	0.074
	0.183	0.923	365	(415)	0.110
	0.436	0.835	155	(250)	0.262
Aerogel[d]	0.085	0.945	(785)[e]	700±100	0.051
	0.190	0.90	(355)	430±65	0.114
	0.455	0.79	(145)	180±45	0.273
	0.825	0.73	(80)	120±25	0.495

[a]Calculated with the assumed value $l_b=20$ Å for the 8CB boundary layer thickness [41].
[b]L values in parentheses for aerosils are estimated by interpolation in a plot of $1/L$ -versus- ρ_S values for aerogels.
[c]Mechanically mixed sample.
[d]References [6,27].
[e]l_0 values for aerogels are estimated using $2/a\rho_S$ and assuming $a=300\ m^2\ g^{-1}$ is also valid for aerogels [28].

below and above $\rho_S=0.1$ are very important points that will be discussed in Sec. IV B.

III. GELS FORMED BY 8CB+AEROSILS

A. Phenomenological description

For all the 8CB+aerosil dispersions studied here, the system forms a weakly connected network gel that is thixotropic. Since the aerosil particles are hydrophilic with a high surface density of hydroxyl groups, they can hydrogen bond to each other easily in an organic medium such as 8CB [17,25]. Thus it is not surprising that such H-bonded chains of particles can break under shear stress and reform quickly (<1 sec) when the stress is removed or relieved. However, in the absence of shear stresses, a slab of any of these gels cut for x-ray studies maintained its shape for long periods of time even when the 8CB was in its I phase [23]. The ability of our 8CB+aerosil dispersions to gel at densities as low as $\rho_S=0.022\ g\ cm^{-3}$ is completely consistent with studies of gel formation for 120-Å-diam hydrophilic aerosil particles in n-decane [25]. In the latter case, the critical value of the silica volume fraction ϕ_S is 0.012 (concentration where the static shear modulus G_0 first becomes nonzero) and G_0 increases linearly with ϕ_S to $1.2\times10^2\ N\ m^{-2}$ when ϕ_S is 0.04. As shown below, the pore volume fraction ϕ (porosity) is 0.990 for our $\rho_S=0.022$ sample and thus $\phi_S=1-\phi=0.01$, which should be very close to the critical gelation value for 8CB+aerosils.

It is obvious from the very low critical ϕ_S value that the gel network in 8CB+aerosils is not a random-walk percolation pattern, for which a minimum coordination number N of 3 is required to generate a volume filling structure [25]. For $N=3$ and random site percolation, the critical threshold probability is $P_c=0.5$ [25], which implies a much larger ϕ_S(crit) than our observed value of ~0.01. The reason for this disagreement with percolation is clearly the ability of the silica particles to diffuse, attract each other, and form long H-bonded chains with only moderate branching. Thus a kinetic model such as those used for polymer chain growth is more appropriate than percolation to model gel formation from aerosil particles.

A summary of structural parameters describing both 8CB +aerosil and 8CB+aerogel systems is given in Table III. For aerosils, the density ρ_S is directly obtained from the preparation masses m_S and m_{LC} of silica and 8CB liquid crystal and the density ρ_{LC} of pure 8CB: $\rho_S=(m_S/m_{LC})\rho_{LC}\cong(m_S/m_{LC})(1\ g\ cm^{-3})$. The volume fraction of ''pores'' ϕ is given by

$$\phi=[1+(\rho_S/\rho_{SiO_2})]^{-1}=(1+0.4545\rho_S)^{-1}, \qquad (8)$$

where we have used the bulk silica density of $\rho_{SiO_2}=2.2\ g\ cm^{-3}$ for the aerosil particles. The mean aerosil void size (equal to the mean LC length scale) l_0 is given by $l_0=2/a\rho_S$, where a is the specific silica area ($a=300\ m^2\ g^{-1}$ for DeGussa type 300 Aerosil [17]). For aerogels, the direct experimental density is the density ρ of the dry (empty) gel and ρ_S can be calculated from $\rho^{-1}=\rho_S^{-1}+\rho_{SiO_2}^{-1}$. The ρ and ρ_{SiO_2} values given in [6] were used to obtain the ρ_S aerogel entries in Table III [26]. Values of l_0 were estimated for the aerogels by assuming that $a=300\ m^2\ g^{-1}$ is also valid for aerogel samples [27]. (Another measure of the LC mean free path length, obtained from SAXS studies of rigid aerogels, is the average pore chord L.) We have estimated L for the 8CB +aerosil samples by interpolation in a plot of $1/L$(aerogel) versus ρ_S. These two measures of the LC length scales, the mean void size l_0 and the average pore chord L, are quite similar in both aerosils and aerogels; differences are presumably due to different specific areas [28]. Finally, the last col-

umn in Table III gives the values of $p=V_b/V_0$, where V_b is the volume of a LC boundary layer in ''contact'' with the silica surface and V_0 is the total LC volume. Now $V_b/V_0 = l_b A/V_0$, where l_b is the thickness of the boundary layer (typically on the order of a molecular length) and A is the total silica surface area. Note that $A/V_0=S/\phi=a\rho_S$, where $S=A/V_T$ is the surface-to-volume ratio in cm^{-1} and ϕ is the porosity (ratio of LC volume V_0 to the total volume V_T). Thus we find $p=l_b a\rho_S=2l_b/l_0$; this quantity is the analog of the quenched random spin site fraction in random-field magnets [29].

Note that $\rho_S=2/a_S l_0$ for aerosils and $\rho_S=2/a_g L$ for aerogels, where a_S and a_g are the specific areas of aerosils and aerogels, respectively [30]. Since a_S is assumed constant for a series of 8CB+aerosil systems, ρ_S is proportional to an inverse LC ''pore'' length for aerosils and thus $\rho_S \propto p$, which makes an attractive experimental variable. See, for example, analogous plots of various quantities versus $1/L$ for the 8CB +aerogel system [6].

In view of the thixotropic nature of the gels formed in 8CB+aerosil samples, where the static shear modulus G_0 rises linearly from zero at a critical porosity $\phi(\text{crit})\cong 0.99$ to a low value such as 1.2×10^2 N m^2 [25] at $\phi=0.96$ (i.e., $\rho_S=0.092$), one would expect that disorder in low-ρ_S samples would anneal to some degree. Such partial annealing, achieved by breaking and reforming H-bonded silica chains, could relieve static smectic and nematic elastic strains and some strains caused by dislocations without changing the overall distribution of silica. However, local rearrangement of the silica particles in the gel network will not anneal local orientational disorder, which is related to the surface field (interaction of the philic SiO_2 surface with the boundary layer of 8CB) and remains quenched. For a silica surface covered with hydroxyl groups, the 8CB molecular axis is expected to be perpendicular to the surface (hedgehoglike configuration) [31]. For 8CB+aerosil samples with sufficiently large ρ_S values, the elastic forces related to N and SmA ordering would not be strong enough to anneal a gel with a large G_0 value. Thus it seems likely that low-ρ_S aerosil samples form ''soft'' gels that can partially anneal elastic strain and high-ρ_S samples form ''stiff'' gels that are more fully quenched and resemble rigid aerogel structures.

B. SAXS procedures and results

Small angle x-ray scattering experiments measure the scattering intensity $I(Q)$, i.e., the differential cross section per unit scattering mass (cm^2 g^{-1}), as a function of the magnitude of the scattering vector $Q=(4\pi/\lambda)\sin(\theta)$, where λ is the incident x-ray wavelength and 2θ is the scattering angle. For a collection of N objects of a characteristic size, one observes a ''knee'' in a log-log plot of $I(Q)$ versus Q. This knee is known as a Guinier region ($QR_g<1$) and can be fit by $I(Q)=NK\exp[-(Q^2R_g^2)/3]$ to extract the characteristic size or radius of gyration R_g. The Guinier region tapers off to a power law $I(Q)=NKQ^{-x}$ at higher Q ($QR_g \gg 1$) where the value of the exponent x is indicative of the dimensionality of the system. Such scattering is common in fractal systems where x can have noninteger values.

There are two distinct types of fractal scattering [32]. For mass fractals, $I(Q)\sim Q^{-D_m}$, where D_m is the fractal dimension that relates the mass M of the object to its length R, $M(R)\sim R^D$. For the case of surface fractals, the scattering goes as $I(Q)\sim Q^{D_{s-6}}$, where D_s is the surface fractal dimension, relating the surface area S to length, $S\sim R^{D_s}$ [32]. For the special case of spherical interfaces, $D_s=2$ giving $I(Q)\sim Q^{-4}$, which is termed Porod scattering [32,33] and arises from the surfaces of nonfractal primary particles. In general, scattering from mass fractals has a power-law exponent value $1<x<3$, surface fractals are characterized by power-law exponents $3<x<4$, and $x=4$ is indicative of a nonfractal interface.

The observed scattering from fractal systems can be quite complex. There are often limited regions of power-law scattering followed by Guinier regimes at lower Q. Here we use the unified approach [34], which breaks a hierarchical structure into multiple structural levels: primary particle, aggregates of primary particle, agglomerates of aggregate, etc. Each structural (ith) level is modeled by two terms, one for the Guinier and one for the higher Q power law [34]

$$I(Q)\cong\sum_{i=1}^{n}\{G_i\exp(-Q^2R_{gi}^2/3)+B_i\exp(-Q^2R_{g(i+1)}^2/3) \times\{[\text{erf}(QR_{gi}/\sqrt{6})]^3/Q\}^{P_i}\}, \quad (9)$$

where n refers to the largest structural level, in our case $n=3$, and P_i the ith level power-law exponent. With the use of Eq. (9), the scattering from a system possessing interrelated multiple-size-scale features can be described over a large range of Q.

SAXS measurements were performed at the University of New Mexico/Sandia National Laboratories Small-Angle X-Ray Scattering Laboratory, employing the 5-m pinhole [35] and Bonse-Hart [36] instruments, which when combined span a wide Q range ($\sim 3\times 10^{-4}\leqslant Q\leqslant 0.6$ Å^{-1} in the present case). Data were collected on a neat 300 aerosil, an aerosil mixed with excess solvent and then dried, and four dispersions of aerosil in 8CB. Measurements were made at room temperature ($\sim$298 K), corresponding to the smectic-A_d phase of 8CB for all 8CB+aerosil samples, and as a function of temperature for one 8CB+aerosil dispersion.

Different methods of sample preparation were investigated in order to determine the effect on the final aerosil structure. One of the pure aerosil samples consisted of a cell filled with the neat or ''fluffy'' aerosil powder, having a tapped density $\rho\cong 0.04$ g cm^{-3}. The other pure aerosil sample was a dry gel prepared by a method analogous to that used for the dispersions (sonicated dispersion in acetone, followed by slow evaporation of the solvent). This sample had a density of 0.18 g cm^{-3} and is denoted as ''collapsed'' since in the absence of a liquid crystal large surface tension forces at the solvent-vapor interface will tend to collapse the aerosil aggregates on drying. The investigated dispersions had densities ρ of 0.051, 0.100, 0.117, and 0.169 g cm^{-3} (corresponding to ρ_S values of 0.052, 0.106, 0.124, and 0.183 g per cm^3 of LC). The lowest- and highest-density samples were prepared in exactly the same manner as the calorimetric samples. No solvent was used in preparing the two intermediate density samples: the $\rho_S=0.106$ sample was mechanically mixed and the $\rho_S=0.124$ sample was sonicated.

Figure 13 displays log-log plots of the SAXS $I(Q)$ data

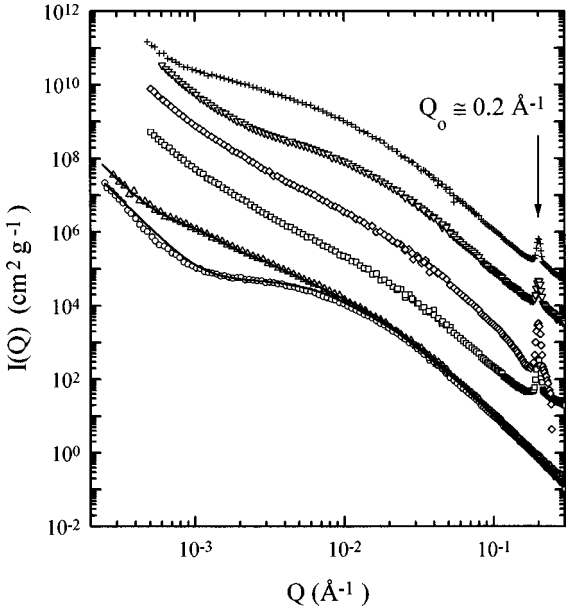

FIG. 13. SAXS absolute intensity curves at ~298 K for ''fluffy'' 300 aerosil (△), ''collapsed'' aerosil (○), and four 8CB +aerosil samples, where the data are scaled upward by factors of 10, 500, 1000, and 10^5 with increasing ρ_S. The latter have silica densities ρ_S of 0.052 (□), 0.106 mechanically mixed (◇), 0.124 sonicated without solvent (▽), and 0.183 (+). The solid lines for the pure aerosil samples represent fits with Eq. (9). In all 8CB +aerosil samples, a smectic 8CB peak is observed at Q_0.

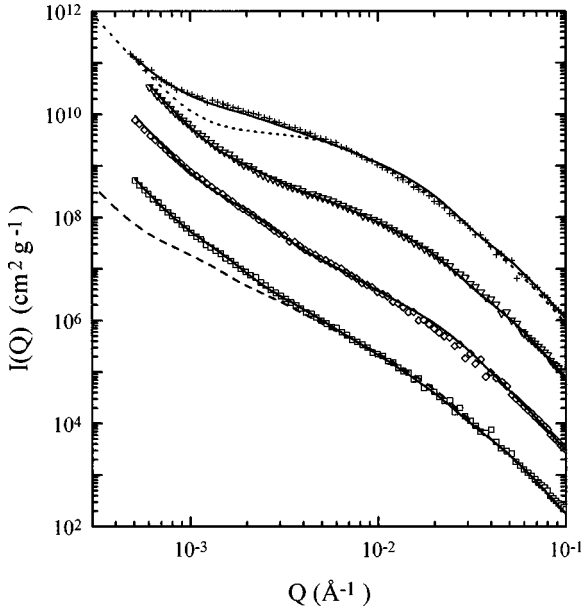

FIG. 14. Fits (solid lines) of the four 8CB+aerosil SAXS curves with Eq. (9). The dashed line represent the fluffy 300 aerosil curve and the dotted line the collapsed 300 aerosil scaled up by a factor of 15 and 9×10^4, respectively, to overlay the high-Q region of the $\rho_S=0.052$ and 0.183 data. The symbols and scaling factors are the same as in Fig. 13.

measured at room temperature for the six samples. For the samples containing 8CB, a Bragg-like peak appears at $Q_0 \cong 0.2$ Å^{-1}, corresponding to a smectic layer thickness $d = 2\pi/Q_0 = 31.4$ Å, in good agreement with published results [37]. As can be seen in Fig. 13, all data show the same shape over the range $0.01 < Q < 0.1$ Å^{-1}, indicating a common particle size and morphology. Below $Q \cong 0.01$ Å^{-1}, significant differences are seen, which, as discussed below, relate to the dimension of the aggregates formed by the aerosil.

The excellent correspondence of the high-Q shape of the SAXS curves for the two pure aerosil samples is demonstrated in Fig. 13, where both the collapsed and fluffy aerosil SAXS data are in absolute intensity units. The solid lines fitting these pure aerosil data were obtained with Eq. (9) for three structural levels: a primary particle, an aggregate of the primary particles, and an agglomerate of the aggregates. Analysis of the unprocessed fluffy 300 aerosil indicates a primary particle with $R_g = 82$ Å and a nonfractal surface morphology. For a spherical particle, where $R_g^2 = 3R^2/5$, this would correspond to an effective diameter of ~212 Å. This suggests that individual, 70-Å-diam, aerosil particles fuse together during the manufacturing process to form a larger, 212-Å-diam, primary particle. These primary particles form a multiparticle diffusion-limited mass fractal aggregate of dimension $D = 1.90 \pm 0.01$. It is difficult to ascertain the maximum size of the mass fractal aggregate since the Q^{-4} feature in the low-Q area (which most likely arises from large silica agglomerates) hinders such determination; however, we estimate the minimum aggregate size to be 4400 Å. The size of the agglomerate could not be estimated since the Guinier region lies at much lower Q than is accessible here and only the beginning of a power-law region is observed. However, the agglomerate is likely macroscopic in extent, a feature of all our aerosil samples. The collapsed aerosil sample was analyzed in a similar manner, with the primary particle size fixed at 212 Å ($R_g = 82$ Å) in view of the similar scattering profiles at high Q. Here capillary forces collapse the structure of the aerosil as the solvent is removed in an exact analogy to xerogels. The most dramatic feature of these data is the almost Q-independent behavior in the range $0.001 < Q < 0.01$ Å^{-1}, which suggests a collapse of the mass fractal aggregate into smaller, denser, aggregates ~660 Å in diameter. A Q^{-4} feature appears in the low-Q region, again arising from the agglomerates of the mass-fractal aerosil aggregates [38]. The aggregate collapse does not appear to be complete since the best fit with Eq. (9) includes a small remnant of a mass fractal with dimension $D = 2.0 \pm 0.2$.

The scaled SAXS curves for the 8CB+aerosil samples along with two scaled curves for the fluffy and collapsed 300 aerosils are shown in Fig. 14 for comparison. The solid lines are the fits with Eq. (9) over three structural levels with the primary particle fixed at 212 Å. As no attempt was made to fit the region of the smectic peak, the data were analyzed over the range $0.0004 < Q < 0.1$ Å^{-1} to avoid any influence of this peak. The two pure aerosil curves are also shown in order to demonstrate the data overlap in the high-Q region. At low aerosil densities ($\rho_S = 0.052$ and 0.106), the entire scattering curve resembles that of the fluffy aerosil sample, whereas the higher density samples ($\rho_S = 0.124$ and 0.183) have scattering curves more akin to that of the collapsed aerosil sample. Analysis reveals the formation of mass fractal aggregates with $D = 2.18 \pm 0.03$ for $\rho_S = 0.052$ and 0.106 samples, with average aggregate sizes of 3675 and 2440 Å, respectively. As the aerosil density was increased above 0.1 g cm^{-3}, the mass fractal dimension begins to decrease, suggesting a partial collapse of the aggregate. For the ρ_S

$=0.124$ and 0.183 samples, the mass fractal dimensions are $D=1.46\pm0.09$ and 1.24 ± 0.05, with aggregate sizes of 2240 and 6330 Å, respectively. The anomalously large aggregate size for the 0.183 sample arises from the influence of the agglomerate scattering in the analysis. Essentially, for high-density samples, there is not enough liquid left to prevent the formation of menisci that produce high surface tension and collapse the aerosil structure as the solvent evaporates.

It was not possible to obtain reliable pore chord lengths L from the SAXS data, as was achieved in the analysis of empty aerogels in Ref. [6], because of the sensitivity of L values to the absolute intensity scale. The absolute scattering intensity is only known to within 10% in the present study, leading to very large uncertainties in L. However, from the scattering profiles, it is clear that an aerogel-like morphology exists for the aerosil structures and accounts for the similar mean void sizes as determined by aerogel interpolation and our geometrical estimate.

The $\rho_S=0.124$ 8CB+aerosil sample was studied as a function of temperature in order to determine if the liquid crystal structure influences that of the aerosil. SAXS curves were obtained at 298 K (SmA_d phase of 8CB), 309 K (N phase), and 323 K (I phase). All three scattering profiles overlay each other very well, indicating that the aerosil structure is essentially independent of temperature, hence the LC phase, for the 8CB+aerosil samples. Note that all calorimetric and SAXS studies were conducted without an external magnetic or electric field, which may alter the aerosil structure [23]. Thus our SAXS study has determined that the present 8CB+aerosil system differs from the 8CB+aerogel system only in the rigidity of the gel structure.

IV. DISCUSSION

The thermodynamic behavior of the 8CB+aerosil samples in the low-ρ_S regime is in stark contrast to the smooth smearing of the phase transition behavior seen in all 8CB+aerogel samples. Since the materials and structures involved in both systems are identical, 8CB as the liquid crystal and a silica network with OH surface groups, the difference in the observed behavior must be the result of the rigidity of the random boundary conditions experienced by the liquid crystal. The three main observations to be explained are (i) for the range $0<\rho_S<0.1$, the N-SmA and N-I transitions in aerosil dispersions shift to lower temperatures faster with increasing ρ_S than is observed in aerogel samples; (ii) two first-order C_p peaks are observed in the N-I coexistence region and the second-order $\Delta C_p(NA)$ evolves towards 3D XY universality for aerosil samples with $\rho_S<0.1$, and (iii) above a crossover silica density of $\rho_S\approx0.1$, 8CB+aerosil samples exhibit shifts in the C_p peak temperatures and decreases in the integrated enthalpies very similar to those observed for 8CB+aerogel samples. In this high-ρ_S regime, the N-I transition remains weakly first order, but the N-A feature becomes a strain-smeared nontransition with a nonsingular rounded $\Delta C_p(NA)$ peak and a greatly reduced $\Delta C_p(NA)$ maximum value.

It should be noted that a single-pore model [1] is clearly not applicable to these 8CB+aerosil samples in view of the low silica concentrations and the open network structures. Although the theory of random-disordered systems has matured, especially in recent years, experiments continue to outstrip theory in such systems. Thus we confine ourselves to an interpretation based on analogies with certain basic mechanisms of imposing disorder. We begin by discussing the high-density aerosil regime and its similarities with the aerogel system revealing a consistent picture of quenched elastic-strain effects. This is followed by a discussion of the low-density aerosil regime with the effects observed and the possibility of this being a physical manifestation of a random-field Ising (RFI) system.

A. High-density regime: Quenched elastic strain

Above the crossover aerosil density of 0.1 g cm^{-3}, the static ΔC_p of the N-I transition exhibits a single, broad, and rounded peak quite similar to that observed in the aerogel systems. The static $\Delta C_p(NA)$ also shows a greatly suppressed and symmetrically rounded bump. Such behavior suggests elastic-strain smearing of both transitions. Therefore, we will begin by discussing the N-I and N-SmA transition temperature shifts followed by a discussion of the N-I transition enthalpy.

For an elastic-strain (ES) mechanism appropriate for a nematic LC, the transition temperature shifts are proportional to R^{-2}, where R is the effective radius of curvature of the elastic strain or distortion. Given the completely random nature of the void geometry, all elastic modes are present and a single elastic constant approximation seems appropriate. Thus the N-I transition temperature shift is given in a mean-field elastic-strain theory by [1,39]

$$T_{NI}(R)=T_{Ni}(\text{pure})-\tfrac{1}{2}(K/a_0)(2\pi/R)^2, \qquad (10)$$

where K is the effective elastic constant and a_0 the leading-order Landau coefficient. With typical values for 8CB [1] of $K\approx4.5\times10^{-11}$ N and $a_0=0.18\times10^6$ J K^{-1} m^{-3}, the second term in Eq. (10) becomes $4.93\times10^5/R^2$, with R in angstroms. Setting $R=l_0$ or $l_0/2$, as is customary in modeling LCs in porous media with regular cylindrical pores, would yield too rapid a variation of T_{NI} with ρ_S: $\Delta T_{NI}=-3$ K at $\rho_S=0.166$ when R is assumed to equal l_0. Given the random nature of the void boundaries in both aerosil stiff gels and rigid aerogels, it is more reasonable to assume $R>l_0$ as the tendency of the LC material would be to minimize the elastic strain (stabilizing the largest possible radius of curvature). Thus the weak concave downward ΔT_{NI} behavior seen in aerogels and high-ρ_S aerosil samples might be explained by mean-field elastic strain effects associated with R values larger than l_0. This is supported by the observation that all transitions in aerogels and the transitions in the high-ρ_S regime of aerosils exhibit single rounded C_p features indicative of strain smearing. The ES curve in Fig. 7 is based on Eq. (10) with $R=5l_0$ and an empirical offset of -0.6 K to account for the saturated behavior of the low-ρ_S regime; see Sec. IV B.

The behavior of the N-SmA transition temperatures is qualitatively similar to that for T_{NI}. Since the N-SmA transition is second order in pure bulk 8CB, one can consider the possible applicability of finite-size scaling theory [40]. This theory predicts among other things a reduction in the value of $\Delta C_p^{\max}(l_0)$ and a shift in T_C, $\Delta T_C\equiv T_C(\infty)-T_C(l_0)$,

where $T_C(\infty)$ is the bulk critical temperature and $T_C(l_0)$ is that in a finite sample of size l_0. These changes are given by $\Delta T_C \propto l_0^{-1/\nu}$ and $\Delta C_p^{\max}(l_0) \propto l_0^{\alpha/\nu}$, where ν is the bulk critical correlation length exponent and α is the bulk heat capacity exponent. For reasons described in detail in Ref. [6], such finite-size scaling does not agree with the experimental C_p data for 8CB in aerogels and we are skeptical about the use of finite-size scaling ideas in the interpretation of 8CB +aerogel x-ray data [4]. The same arguments can be used to rule out finite-size scaling theory as a description of the 8CB +aerosil heat capacity data. First, the theory predicts that $\Delta C_p(l_0)$ as a function of $T-T_C(l_0)$ should be independent of l_0 except for a narrow range of $|t|$ values less than $|t_0|$ where the correlation length $\xi \geqslant l_0$. However, this is contradicted by the data in Fig. 5. Second, finite-size theory predicts $\Delta T_C \sim l_0^{-1/\nu} \sim \rho_S^{1/\nu}$ since $l_0 \sim \rho_S^{-1}$ for aerosil samples and $1/\nu$ for 8CB lies in the range 1.50–1.96 ($1/\nu_\parallel = 1.50$ to $1/\nu_\perp = 1.96$) [6]. This prediction disagrees seriously with the ΔT_C vs ρ_S plot in Fig. 8. Third, the maximum value of $\Delta C_p(NA)$ for 8CB+aerosil samples is quite well represented by $\Delta C_p^{\max}(NA) = 0.041 \rho_S^{-1}$, which has the same kind of ρ_S dependence as the 8CB+aerogel samples where $\Delta C_p^{\max}(NA) = 0.015 \rho_S^{-1}$ [6]. This empirical dependence differs markedly from the theoretical prediction $\Delta C_p^{\max}(NA) \sim l_0^{\alpha/\nu} \sim \rho_S^{-0.5 \pm 0.05}$. See Ref. [6] for further details. Thus the *N*-Sm*A* behavior supports the idea that strain smearing dominates the high-density regime.

It is likely that the same sort of elastic-strain mechanism as developed above for T_{NI} also applies to the shift in T_{NA} for the stiff gels, but Eq. (10) is not useful since (i) mean-field theory is not valid for *N*-Sm*A* transitions, (ii) appropriate values of K and a_0 are not known, and (iii) the observed curvature of the experimental $T_{NA}-\rho_S$ plot has an opposite sign from that for $T_{NI}-\rho_S$ and that given by Eq. (10). It is possible that the sort of elastic-strain model needed involves the creation of short-range Sm*A* glass layers in a nematic glass [11].

Two related theories to consider for dealing with the density dependence of the first-order *N*-*I* transition enthalpy $\Delta H_{\rm tot}(NI) = \delta H_{NI} + \Delta H_{NI}$ are a pinned-boundary-layer (PBL) and a random-field (RF) model. In both models, one assumes that a fraction p of the LC material is quenched and does not participate in any ordering transition. In effect, this partitions the LC material into ordering and nonordering masses. We show below that neither of these models is applicable to the present data for $\Delta H_{\rm tot}(NI)$ or for δH_{NA} in the high-ρ_S regime.

For the PBL model, the orientational anchoring at the silica surface is so strong that the LC material in the boundary layer is quenched and the remaining LC behaves as pure bulk material. Assuming that the LC density is constant and the specific area of the aerosil is independent of concentration (valid in a dilute mixture), the total apparent *N*-*I* transition enthalpy given by the PBL model is $\Delta H_{\rm tot}({\rm PBL}) = \Delta H_{\rm tot}(0)(1-p)$. For the RF model, the quenched LC is simply distributed randomly in space leading to an additional reduction of the average order in the remaining material affecting the latent heat of the *N*-*I* transition. At the mean-field level, the *N*-*I* latent heat is given by $\Delta H = \frac{1}{2} a_0 Q_N^2 T_{NI}$, where Q_N is the order of the N phase at T_{NI} and a_0 is the leading-order Landau–de Gennes free-energy expansion coefficient [39] with the orientational order of the coexisting I phase at T_{NI} taken as zero. Using a mean-field formalism for random-field disorder on a nematic, Maritan, Cieplak, and Banavar [29] derive the average orientational order as $\overline{Q}(p) = Q[\rho_S, T_{NI}(\rho_S)] = Q[0, T_{NI}(0)](1-p)$. The expression for the *N*-*I* transition temperature shift due to quenched random-field disorder is $T_{NI}(\rho_S) = T_{NI}(0)(1-p)$ [29], which is the effect of random dilution (RD). Substituting into the expression for ΔH above yields $\Delta H_{\rm tot}({\rm RF}) = \delta H(p) + \Delta H(p) = \delta H(0)(1-p) + \Delta H(0)(1-p)^3$.

Although the RF model predicts a somewhat weaker decrease in $\Delta H_{\rm tot}(\rho_S)$ than the PBL model, both derivations suffer from the same difficulties. The reduction in the order by a factor of $1-p$ arises from a fraction of the material that is fully quenched. This decreases δH as well as ΔH, which is not observed experimentally. Also, the transition temperature shift is zero for the PBL model, while the RF model predicts far too rapid a *N*-*I* transition temperature decrease with increasing ρ_S than is observed for $\rho_S > 0.1$. Thus, neither the PBL nor the RF model for $\Delta H_{\rm tot}(\rho_S)$ appears to be a physically reasonable description of aerogel or aerosil ($\rho_S > 0.1$) perturbations on the *N*-*I* phase transition enthalpy.

A more appropriate model of $\Delta H_{\rm tot}(\rho_S)$ for the *N*-*I* transition involves the effect of surface-induced order converting the isotropic into a paranematic phase. Surface-induced nematic order is known to decay over hundreds of angstroms away from a surface [1,38], allowing one to volume average the boundary layer nematic order Q_b with the remaining void volume order $Q(0)$. Since Q_b is not quenched, we can consider the effect on the latent heat alone, which we write, at the mean-field level, as $\Delta H = \frac{1}{2} a_0 (Q_N^2 - Q_I^2) T_{NI}$, where we explicitly include the orientational order in the I phase at T_{NI}. The volume average orientation order parameter at T_{NI} gives $\overline{Q}_I = Q_I(0)(1-p) + Q_b p$ in the coexisting I phase and $\overline{Q}_N = Q_N(0)(1-p) + Q_b p$ in the coexisting N phase. Note that $Q_I(0) = 0$ and $Q_N(0) \cong 0.3$ are the pure 8CB long-range order parameters for both phases at T_{NI}. Thus, at the *N*-*I* transition, $\overline{Q}_N^2 - \overline{Q}_I^2 = Q_N^2(1-p)^2\{1 + 2Q_b p/Q_N(1-p)\}$. We take the elastic-strain effects as an appropriate description of the shift in T_{NI} given by $T_{NI}(\rho_S) = T_{NI}(0)(1 - 0.0142\rho_S^2)$ [see Eq. (10)], with R is taken as $5l_0 = 10/a\rho_S$, as observed experimentally. Taking $p = l_b a \rho_S \cong 0.6\rho_S$ for 8CB+aerosil where $l_b \cong 20$ Å for 8CB [37,41], the suppression of $\Delta H_{\rm tot}(\rho_S) = \delta H_{NI}(0) + \Delta H_{NI}(\rho_S)$ for this purely mean-field (MF) model is given by

$$\Delta H_{\rm tot}(\rho_S) = \delta H_{NI}(0) + \Delta H'(0)(1-0.6\rho_S)^2 \times [1 + 1.2 Q_b \rho_S / Q_N(1-0.6\rho_S)] \times (1 - 0.0142\rho_S^2), \quad (11)$$

where $\delta H_{NI}(0)$ is 5.43 J g^{-1} (the unperturbed ΔC_p wing contribution) and $\Delta H'(0) = 2.25$ J g^{-1}. The quantity $\Delta H'(0)$ is the sum of the pure 8CB latent heat (2.10 J g^{-1}) and a small portion of the wing enthalpy δH_{NI} very close to T_{NI} in pure 8CB (0.15 J g^{-1}). The latter quantity corresponds to the enthalpy $\delta H_{NI}(0) - \delta H_{NI}({\rm sil})$, which appears as latent heat in sil samples due to the broader $N+I$ coexistence re-

gion; see Fig. 3. Equation (11) has only one adjustable parameter Q_b and the solid line in Fig. 10 represent the best fit achieved with $Q_b=-0.15$.

The above MF form seems to model the behavior of $\Delta H_{\rm tot}(\rho_S)$ reasonably well. The negative sign for Q_b can be understood if the local director near the silica surface is homeotropic and the nematic director in the void volume is parallel to the silica strands. This is quite reasonable in our system where no external fields compete with the surface-induced order since homeotropic order extending from the silica strands throughout the void volume would result in a huge splay penalty. The most likely result is an ''escaped-radial'' director structure that would be the analog to that observed in Anopore confinement [42]. Note that Eq. (11) predicts for $Q_b=-0.15$ that $\Delta H_{\rm tot}(NI)\rightarrow\delta H(0)$ at $p\cong 0.63$ ($\rho_S=1.05$ g cm^{-3}) corresponding to $\phi=0.48$, which would be achieved in a regular space-filling structure with coordination number $N\cong 5$ [26]. Finally, one must assume that the N-I energy fluctuation effects at any temperature are the same for 8CB in the boundary layer and in the remainder of the void volume and that both average order parameters $\overline{Q}_b$ and $\overline{Q}(0)$ develop in the same way as a function of T below T_{NI}. This is required to leave the shape and integrated area (δH) of the C_p wings independent of ρ_S. This too seems reasonable given that the magnitude of Q in the boundary layer is only a factor of 2 smaller than in the void at T_{NI}. Unfortunately, the nature of fluctuation effects near the N-I transition in pure liquid crystals is still not well understood (largely due to the weak first-order character of all N-I transitions), thus the details of this effect on the C_p wings remain ambiguous. Note that in the MF model of $\Delta H_{\rm tot}(\rho_S)$, randomness plays a comparatively minor role, relegated more to the N-I transition temperature shift, which, as previously described, is a relatively small effect.

B. Low-density regime: Annealed elastic strain

The low-density aerosil regime exhibits several types of behavior that do not fit the quenched elastic-strain picture described above for stiff or rigid random confining systems. In fact, the observed sharpness of both the N-I and N-SmA transitions along with their simultaneous rapid shift to lower temperatures appear to be better describe by a purely RFI model.

We consider the RFI model to be a viable approximation in the low-ρ_S soft-gel regime because the aerosil chains can move and anneal elastic strains. The N-SmA heat capacity exponent α evolving toward zero (or 3D XY behavior) if $\alpha_{\rm pure}>0$ and remaining unaffected if $\alpha_{\rm pure}<0$, as shown in Fig. 12, would then be understood as a manifestation of the Harris criterion [43] for the evolution of second-order critical behavior in a random field. The present work along with Refs. [10] and [12] would represent its experimental verification. Also, the rapid N-I transition temperature shift appears to be described by the RFI RD model given by $T_{NI}(p)=T_{NI}(0)(1-p)$ [29], where $T_{NI}(0)$ is the N-I transition temperature in the pure LC and p is the fraction of ''quenched'' LC. Again taking $p=0.6\rho_S$ for 8CB+aerosil, one can calculate the dotted RD model line in Fig. 7 with no adjustable parameters. Surprisingly, the T_{NI} shift described by the RFI (RD) model in the low-ρ_S regime does not disappear but appears to transform sharply into a *constant* offset of about -0.6 K at and above 0.1 g cm^{-3}. Recall that the ES transition temperature shift for $\rho_S>0.1$ contained an empirical offset in order to describe the high-ρ_S regime ΔT_{NI}. We have no explanation for this behavior, but it may represent the interplay between the dilution of the ordered phase and the imposed elastic strain. Since the critical behavior of $\Delta C_p(NA)$ is changing in this ρ_S region, no description of δH_{NA} is possible.

Given an annealed elastic strain while preserving the random surface field, the low-ρ_S regime would now appear to closely match the requirements of the RFI model and point to a possibly consistent interpretation for both aerosil and aerogel systems. For aerosils in the low-ρ_S (soft-gel) regime, the silica particles would locally arrange themselves into short sticks that are randomly oriented throughout the sample. This would alleviate (anneal) as much of the elastic strain on the LC as possible and lead to the escaped-radial director structure as discussed for the high-ρ_S regime. The system can then be pictured as a collection of nematic domains that are more or less uniformly aligned along the local aerosil orientation beyond a thin surface layer that is at the center of each nematic domain. The nematic domains can now be thought of as ''spins'' as in an Ising lattice with the aerosil providing a random field for each spin (domain). For the N-I transition, the sharp higher temperature C_p peak would then represent the first-order N-I transition subjected to a random-field, while the more rounded lower temperature C_p peak would represent the elastic strain coarsening as the LC director ''stiffens'' below T_{NI}. The coarsening would only extend over relatively long length scales, essentially between strands of aerosils. The smectic ordering to follow would then occur in domains of uniformly aligned but not saturated nematic order. This would have no effect on the amplitude of the smectic order parameter (which would be more of a random-bond effect) but would randomize its phase, precisely the needed coupling for a random field on a second-order vector order parameter.

For both the rigid aerogel and high-ρ_S (stiff-gel) aerosil, the coarsening of elastic strains now occurs over all length scales. This is the dominant mechanism with the elastic-strain smearing having an effective (average) radius of curvature larger than the mean pore size. Thus the mobility of the aerosil particles at low ρ_S, which allows a local annealing of the elastic strain while simultaneously randomly fixing the nematic director, plays a crucial role.

V. CONCLUSION

A high-resolution ac calorimetric and SAXS study has been carried out as a function of silica concentration on a series of dispersions combining 8CB liquid crystals with type 300 hydrophilic aerosils. Taking the present study together with previous work on many different LC confined systems leads to a general outline of random disorder and confinement effects. The results reported here for the 8CB +aerosil system exemplifies the overall behavior of LC subjected to random disorder.

The effect of aerosil-induced random disorder on LC phase behavior can be categorized into two regimes. The first is typified by rigid aerogel behavior where it appears that all

first- and second-order phase transitions suffer from quenched elastic-strain smearing effects with a radius of curvature of the elastic distortion R taken as much larger than the mean void size. Here both the elastic strain and surface anchoring fields are quenched. Examples include aerogel confined 8CB [2,6], 4O.8 [7], 7O.4 [8], and 8S5 [9]. Other examples include high-ρ_S 8CB+aerosil dispersions presented in this work and in Ref. [10], where the shear modulus of the gel has grown to the point, compared to the elastic modulus of the LC, where it can be considered a stiff gel. In fact, similar behavior differing only in degree of transition temperature shifts and smearing was also observed in Anopore-confined 8CB [42]. Anopore is a noninterconnected uniform (nonrandom) cylindrical porous media with pore size much larger than that in the lightest aerogel studied where R is now related to the pore size due to the pores cylindrical geometry. This leads to a tantalizing conclusion that all LC phase behavior within a ''rigid'' or ''stiff'' confining media may be dominated by quenched elastic-strain smearing effects that destroy long range order and where randomness only introduces a distribution of strains. A quantitative modeling of such systems can then only be achieved by properly accounting for the distribution of elastic strains occurring in the particular confining media. Beginning from a first-principles approach, this behavior may be better described by the model put forth by Radzihovsky and Toner [11] in which, under certain conditions, the N-I transition is converted to a paranematic-nematic glass transition and conversely, the N-SmA transition is converted to a N-SmA glass transition.

The second regime that emerges is the low-density LC +aerosil dispersions, which can be labeled as the soft-gel regime. Here it appears that the second-order N-SmA phase transition C_p remain sharp with its critical behavior evolving toward 3D XY universality in accordance with the Harris criterion [43] while rapidly shifting to lower temperatures. It also appears that first-order phase transitions such as the N-I [10,12,13], SmC-CrB [12], and SmA-CrG [13] phase transitions remain sharper in low-density aerosil mixtures than in any aerogel samples or in high-ρ_S aerosil samples. Also, there exist two C_p features at a first-order N-I phase transition: a very sharp and narrow C_p spike followed at lower temperatures by a more rounded C_p peak. This is exemplified by 8CB+aerosil as shown in this present study. These two features shift rapidly to lower temperatures together with the higher- (lower-) temperature feature decreasing (increasing) in intensity as the silica density increases. All transition temperature shifts are much more rapid in this soft-gel regime than seen in the stiff or rigid gel regime. Also, qualitatively similar behaviors were observed for the critical heat capacity exponent of $\Delta C_p(NA)$, the N-I and N-SmA transition temperature shifts, and the sharpness of $\Delta C_p(NI)$ for 8CB confined to Millipore membranes, a soft porous structure [44]. It is natural to propose that LC within soft-gel systems allows an annealing of the elastic strains responsible for transition smearing but leaves intact a quenched random surface field. The physical picture of the low-ρ_S LC+aerosil mixtures comprised of relatively large nematic domains (spins) having a randomly oriented silica strand at its center determining its orientation (random field) matches the physical picture of the RFI model. Such systems appear to be good experimental candidates to study random disorder and the details of the underlying physics of the random-field Ising model.

ACKNOWLEDGMENTS

We would like to thank H. Haga and L. Radzihovsky for many useful experimental and theoretical discussions. This work was supported at MIT by the MRSEC NSF Program under Grant No. DMR 94-00334. T.R. acknowledges the help of Paul Hubbard in acquiring the SAXS data and the support of Sandia National Laboratories, operated for the U.S. Department of Energy under Contract No. DE-AC04-98A185000. J.M. acknowledges the support of the U.S. Department of Energy under Contract No. W-7405-ENG-36, with the University of California.

[1] *Liquid Crystals in Complex Geometries Formed by Polymer and Porous Networks*, edited by G. P. Crawford and S. Zumer (Taylor and Francis, London, 1996), and references cited therein.

[2] T. Bellini, N. A. Clark, C. D. Muzny, L. Wu, C. W. Garland, D. W. Schaefer, and B. J. Oliver, Phys. Rev. Lett. **69**, 788 (1992); T. Bellini, N. A. Clark, and D. W. Schaefer, *ibid.* **74**, 2740 (1995); T. Bellini and N. A. Clark, in *Liquid Crystals in Complex Geometries Formed by Polymer and Porous Networks* (Ref. [1]), Chap. 19.

[3] X.-I. Wu, W. I. Goldburg, M. X. Liu, and J. Z. Xue, Phys. Rev. Lett. **69**, 470 (1992).

[4] N. A. Clark *et al.*, Phys. Rev. Lett. **71**, 3505 (1993); A. G. Rappaport, N. A. Clark, B. N. Thomas, and T. Bellini, in *Liquid Crystals in Complex Geometries Formed by Polymer and Porous Networks* (Ref. [1]), Chap. 20.

[5] G. S. Iannacchione, S. Qian, D. Finotello, and F. Aliev, Phys. Rev. E **56**, 554 (1997); G. S. Iannacchione, G. P. Crawford, S. Zumer, J. W. Doane, and D. Finotello, Phys. Rev. Lett. **71**, 2595 (1993); **53**, 2402 (1996).

[6] L. Wu, B. Zhou, C. W. Garland, T. Bellini, and D. W. Schaefer, Phys. Rev. E **51**, 2157 (1995), and references cited therein.

[7] Z. Kutnjak and C. W. Garland, Phys. Rev. E **55**, 488 (1997).

[8] H. Haga and C. W. Garland, Liq. Cryst. **22**, 275 (1997).

[9] B. Zhou, G. S. Iannacchione, and C. W. Garland, Liq. Cryst. **22**, 335 (1997).

[10] B. Zhou, G. S. Iannacchione, C. W. Garland, and T. Bellini, Phys. Rev. E **55**, 2962 (1997).

[11] L. Radzihovsky and J. Toner, Phys. Rev. Lett. **78**, 4414 (1997); **79**, 4214 (1997).

[12] H. Haga and C. W. Garland, Phys. Rev. E **56**, 3044 (1997).

[13] H. Haga and C. W. Garland, Liq. Cryst. **23**, 645 (1997).

[14] J. C. LeGuillon and J. Zinn-Justin, Phys. Rev. Lett. **39**, 95 (1977); Phys. Rev. B **21**, 3976 (1980); C. Bagnuls and C. Bervillier, Phys. Lett. **112A**, 9 (1985).

[15] J. Thoen, H. Marynissen, and W. Van Dael, Phys. Rev. A **26**, 2886 (1982).

[16] 8CB in aerogels crystallizes on cooling at 273–278 K in $\rho_S = 0.085$ and 0.19 samples, 271–275 K in a $\rho_S = 0.455$ sample, and 263–268 K in a $\rho_S = 0.825$ sample. See Ref. [4] for further details.

[17] DeGussa Corp., Silica Division, 65 Challenger Road, Ridgefield Park, NJ 07660. Technical data and properties are given in the manufacturer's booklet AEROSILS.

[18] C. W. Garland, Thermochim. Acta **88**, 127 (1985); *Liquid Crystals: Physical Properties and Phase Transitions*, edited by S. Kumar (Oxford University Press, New York, in press), Chap. 6 and references cited therein.

[19] H. Yao, T. Chan, and C. W. Garland, Phys. Rev. E **51**, 4585 (1995).

[20] H. Yao, K. Ema, and C. W. Garland, Rev. Sci. Instrum. **69**, 172 (1998).

[21] G. B. Kasting, C. W. Garland, and K. J. Lushington, J. Phys. (Paris) **41**, 879 (1980); M. Marinelli, F. Mercuri, S. Foglietta, U. Zammit, and F. Scudieri, Phys. Rev. E **54**, 1604 (1996). Small differences in the amplitude ratio A^-/A^+ reported for pure 8CB (0.83–1.11) are completely due to the differences in the correction coefficients $D^{\pm}$ used. The best estimate for A^-/A^+ is 1.00 ± 0.08; see fits for small $|t|$ in Ref. [15].

[22] X. Wen, C. W. Garland, and M. D. Wand, Phys. Rev. A **42**, 6087 (1990).

[23] J.-L. Gallani, R. L. Leheny, and S. Park (private communication).

[24] C. W. Garland and G. Nounesis, Phys. Rev. E **49**, 2964 (1994), and references cited therein.

[25] H. Sonntag and K. Strenge, *Coagulation Kinetics and Structure Formation* (Plenum, New York, 1987), pp. 134–145 and 172–177.

[26] If one were to assume that the silica density in the solid struts is 2.2 g cm^{-3} for all four aerogels studied in [6], the ρ_S values in Table III would decrease (and thus ϕ values increase) by 2.2% for the $\rho = 0.08$ aerogel, 2.8% for the $\rho = 0.17$ aerogel, 5.7% for the $\rho = 0.36$ aerogel, and 0.0% for the $\rho = 0.60$ aerogel.

[27] A. Emmerling and J. Fricke, J. Non-Cryst. Solids **145**, 113 (1992).

[28] If one makes the reasonable assumption that the specific silica area decreases as the aerogel density increases, the agreement between l_0 and L can be significantly improved. Choosing $a = 200$ m^2 g^{-1} for the $\rho_S = 0.825$ aerogel, $a = 250$ m^2 g^{-1} for the $\rho_S = 0.455$ and 0.190 aerogels, and $a = 300$ m^2 g^{-1} for the $\rho_S = 0.085$ aerogel, the resulting l_0 and L values for both aerosils and aerogels agree within 12% in all cases except for the $\rho_S = 0.436$ aerosil where the new $L = 280$ Å value is 36% larger than $l_0 = 155$ Å.

[29] A. Maritan, M. Cieplak, and J. R. Banavar, in *Liquid Crystals in Complex Geometries Formed by Polymer and Porous Networks* (Ref. [1]), Chap. 22; Phys. Rev. Lett. **72**, 4113 (1994).

[30] In Ref. [6] and Refs. [14–17] cited therein $\rho_S = S/a\phi$ yields $\rho_S = 4/aL$ since it was assumed that $S = 4/(L + d_s)$ should be used where d_s is the solid chord length. However, that S expression is only valid for ''closed'' void geometries where the LC resides in tubular or spherical pores. For ''open'' void geometries, where the silica is in sheets, rods (chains), or compact clusters, $S = 2/(L + d_s)$ is correct.

[31] J. Cognard, Mol. Cryst. Liq. Cryst. Suppl. Ser. **1**, 1 (1982).

[32] D. W. Scheafer and K. D. Keefer, Phys. Rev. Lett. **56**, 2199 (1986).

[33] H. Brumberger, *Modern Aspects of Small Angle Scattering* (Kluwer Academic, Boston, 1995).

[34] B. Beaucage, J. Appl. Crystallogr. **28**, 717 (1995).

[35] T. P. Rieker and P. F. Hubbard (unpublished).

[36] T. P. Rieker and P. F. Hubbard (unpublished).

[37] D. Davidov, C. R. Safinya, M. Kaplan, S. S. Dana, R. Schaetzing, R. J. Birgeneau, and J. D. Litster, Phys. Rev. B **19**, 1657 (1979).

[38] C. Sorensen, P. W. Schmidt, and T. P. Rieker (unpublished).

[39] P. G. de Gennes and J. Prost, *The Physics of Liquid Crystals*, 2nd ed. (Clarendon, Oxford, 1993), and references therein.

[40] M. E. Fisher and A. E. Ferdinand, Phys. Rev. Lett. **19**, 169 (1967); M. E. Fisher and M. N. Barber, *ibid.* **28**, 1516 (1972); W. Hahn and V. Dohm, *ibid.* **61**, 1368 (1988).

[41] M. Hara, Y. Iwakabe, K. Tochigi, H. Sasabe, A. F. Garito, and A. Yamada, Nature (London) **344**, 228 (1990). Since 8CB molecules are anchored perpendicular to a philic silica surface, we have taken the boundary layer thickness I_b to be the extended length of a single 8CB rather than the partial bilayer thickness of ~31.6 Å [37].

[42] G. S. Iannacchione and D. Finotello, Phys. Rev. Lett. **69**, 2094 (1992); Phys. Rev. E **50**, 4780 (1994), and references therein.

[43] A. B. Harris, J. Phys. C **7**, 1671 (1974); J. T. Chayes, L. Chayes, D. S. Fisher, and T. Spencer, Phys. Rev. Lett. **57**, 2999 (1986); A. Weinrib and B. I. Halperin, Phys. Rev. B **27**, 413 (1983); A. Weinrib, *ibid.* **29**, 387 (1984).

[44] S. Qian, G. S. Iannacchione, and D. Finotello, Phys. Rev. E **53**, R4291 (1996).